Title: (101/135 characters)

Estrogen Signaling in Arcuate *Kiss1* Neurons Suppresses a Sex-Dependent Circuit That Promotes Dense Strong Bones in Female Mice

Authors: Candice B. Herber[1†], William C. Krause[1†], Liping Wang[2], James R. Bayrer[3], Alfred Li[2], Matthew Schmitz[4], Aaron Fields[5], Breanna Ford[6], Michelle S. Reid[7], Daniel K Nomura[6], Robert A. Nissenson[2], Stephanie M. Correa[1,7‡], and Holly A. Ingraham[1]

Affiliations:
[1] Department of Cellular and Molecular Pharmacology,
[2] VA Medical Center Endocrine Unit and Bone Imaging Core Facility
[3] Department of Pediatrics
[4] Graduate Program in Developmental Biology, School of Medicine
[5] Department of Orthopedic Surgery,
School of Medicine Mission Bay Campus
University of California San Francisco,
San Francisco, California 94158, USA

[6]Department of Nutritional Sciences and Toxicology
University of California, Berkeley
Berkeley, California 94720, USA

Present Address:
[7]Department of Integrative Biology and Physiology
University of California Los Angeles
Los Angeles, California 90095, USA

† Equal Contribution

‡Co-corresponding Authors: stephaniecorrea@ucla.edu and holly.ingraham@ucsf.edu

Classification Major: Biological Sciences
Classification Minor: Medical Sciences or Physiology

Abstract

(227/250 Words) Hypothalamic neurons in the medial basal hypothalamus (MBH) have been shown to regulate modest changes in bone density in both males and females. Central estrogen signaling has also been implicated in altering bone mass in intact, but not estrogen-depleted female mice. While estrogen-responsive hypothalamic modules have been defined for coordinating energy expenditure and reproduction in females, the precise neurons involved in an estrogen-dependent putative brain-to-bone pathway remain poorly defined. Here, we ablate estrogen receptor alpha (ERα) in the entire MBH and find a massively dense bone phenotype only in female mice. Loss of ERα in the female MBH increases markers of bone morphogenic protein (BMP) signaling and osteoblast differentiation, resulting in exceptionally strong trabecular and cortical bones, whose density surpasses other reported mouse models. Acute ablation of ERα in the ARC by stereotaxic guided deletion increases bone mass in both intact and estrogen-depleted females, confirming the central role of estrogen signaling on skeletal homeostasis. Finally, we find that ablating ERα activity in *kisspeptin* (*Kiss1*) neurons is sufficient to recapitulate the effects on bone, identifying Kiss1 neurons as a critical node in this powerful neuroskeletal circuit. We propose that this newly identified female brain-to-bone pathway exists as a homeostatic regulator to divert calcium and energy stores from bone building when energetic demands are high. Our work reveals a previously unknown target for the treatment of age-related bone disease.

Significance Statement

Our study defines central regulation of bone metabolism, alongside reproduction and energy balance, as a fundamental determinant of female physiology. Estrogen signaling in the brain is beneficial for energy expenditure and reproduction in female mice. Using three independent and intersectional strategies, we discovered that estrogen signaling in hypothalamic *kisspeptin* neurons is also a powerful negative regulator of bone metabolism. Ablating ERα in *kisspeptin* neurons results in a massive female-specific increase in bone density leading to exceptionally strong bones. When this neuroskeletal homeostatic circuit is broken in older and “post-menopausal” female mice, bone health improves. Our work provides a platform for further mechanistic investigations that might eventually provide new opportunities to counteract age-related osteoporosis in both women and men.

Key Words:
Kisspeptin Neurons
Central estrogen signaling
Sex-dependent
Anabolic bone metabolism
Brain-bone pathway

Introduction

The sex steroid hormone estrogen is critical for balancing energy allocation and expenditure to ensure maximal reproductive fitness. Peripheral estrogen is an important regulator of skeletal homeostasis. In rodents, circulating 17β-estradiol (E2) actively promotes anabolic bone metabolism. Indeed, chronic administration of E2 to ovariectomized (OVX) or intact females at low (1) or high doses (2) leads to a significant increase in trabecular bone mass. On the other hand, central estrogen signaling negatively impacts female bone metabolism as suggested by the modest increase in bone mass following central loss of estrogen receptor alpha (ERα) using the brain-specific, but problematic *Nestin-Cre* (3, 4). Estrogen-dependent augmentation of cortical bone mass bone also has been reported after deleting ERα using the non-inducible and developmentally promiscuous *POMC-Cre* (1, 5). In both genetic models, these bone phenotypes vanish in OVX females suggesting that compensatory increases in circulating sex steroids account for the increased bone mass following loss of central estrogen signaling. Independent of estrogen signaling, manipulating NPY or AgRP ARC neurons also modestly influences bone metabolism, at least in male mice (6, 7).

Within the medial basal hypothalamus (MBH) ERα is highly enriched in two anatomically and functionally distinct neuronal clusters, the arcuate nucleus (ARC) and the ventral lateral region of the ventromedial hypothalamus (VMHvl). Estrogen signaling in the female MBH promotes a catabolic energy state by regulating distinct aspects of energy balance (8-10) Indeed, conditional mouse models in which ERα is deleted in some, but not all, ARC or VMHvl neurons suggest that these two estrogen-responsive brain modules separately regulate distinct aspects of energy balance (8, 9). Partial loss or pharmacological blockade of ERα in the VMH lowers energy expenditure by decreasing brown adipose tissue (BAT) thermogenesis (9, 11) and lowering physical activity (8), respectively. Within the ARC, ERα is expressed in multiple cell types, each expressing a signature neuropeptide or

neurotransmitter system. Estrogen signaling in the POMC lineage is thought to limit food intake as inferred from deletion of ERα using the POMC-Cre (*Esr1*$^{POMC\text{-}Cre}$) (9, 11, 12). Most *kisspeptin* (*Kiss1*) neurons in the ARC also express ERα. Kisspeptin itself regulates puberty and fertility in both male and female mice (13, 14), as well as in humans (15). However, ERα signaling dynamically regulates *Kiss1* ARC neurons by silencing *Kiss1* expression and restraining the onset of female, but not male pubertal development (16). Deleting ERα using *Kiss1-Cre* upregulates *Kiss1*, accelerates pubertal onset in female mice, and increases inhibitory firing of Kiss1^{ARC} neurons (17, 18). While ERα is excluded from AgRP neurons (19), these nutritional sensing neurons project and inhibit *Kiss1* ARC neurons (20). Tyrosine hydroxylase (TH) neurons in the ARC also express ERα and play an orexigenic role on energy balance (21).

Given the cellular complexity of estrogen responsive neurons in the ARC and VMHvl, we leveraged the *Esr1*$^{Nkx2\text{-}1Cre}$ mouse model (8), in which all ERα in the MBH is eliminated via *Nkx2-1*-driven Cre recombinase (8) to ascertain how ERα in the ARC and VMHvl influences energy expenditure, reproduction and possibly skeletal homeostasis. We confirmed that any observed phenotypes were neuronal in origin using stereotaxic delivery of AAV2-Cre to acutely ablate ERα in either the ARC or VMHvl in adult female mice. We found that eliminating ERα in the ARC resulted in a robust and sex-dependent high mass bone phenotype. Importantly, we go on to define *Kiss1* neurons as the critical estrogen-responsive subpopulation in the ARC for promoting this remarkable, robust bone mass in female mice.

Results

In *Esr1*$^{Nkx2\text{-}1Cre}$ mice, ERα is efficiently eliminated in the entire MBH in both male and female brains, including the ARC and VMH, but is largely maintained in the anteroventral periventricular nucleus (AVPV), preoptic area (POA), nucleus tractus solitarius (NTS), and

medial amygdala (MeA) (Fig 1A and Supplementary Fig 1A). Deleting ERα in the MBH depleted primordial follicles, and led to female infertility, and uterine imbibition (Supplementary Fig 1B-D), as previously documented (16, 22). Mutant females displayed a small but significant increase in body weight, which was less robust than reported for *Esr1*$^{POMC\text{-}Cre}$ (9), whereas body weights for mutant males decreased (Fig 1B). Food intake was unchanged in both sexes (Fig 1C)

Esr1$^{Nkx2\text{-}1Cre}$ females exhibited a sex-dependent change in energy balance that was entirely absent in male mice. The lean mass of mutant females was significantly higher than control floxed (*Esr1*$^{fl/fl}$) littermates (Fig 1D) and was accompanied by decreased physical activity during the dark phase (Fig 1E and Supplementary Fig 2) and blunted brown adipose tissue (BAT) thermogenesis as evidenced by whitening of BAT and decreased *Ucp1* levels; circulating catecholamines were lower in mutant mice but not significantly so (Fig 1F and Supplementary Fig 2). Serum leptin levels were unchanged (Fig 1G). Thus, these data reveal that central estrogen signaling in this brain region promotes a sex-dependent negative energy state in females in the absence of any change in feeding behavior. This finding implies that the hyperphagia reported for *Esr1*$^{POMC\text{-}Cre}$ mice might result from ectopic activity of POMC-Cre in non-ARC neurons (5).

Strikingly, bone mineral density (BMD), as determined by DEXA (Dual X-ray Absorptiometry), was significantly elevated in *Esr1*$^{Nkx2\text{-}1Cre}$ females, but not males (Fig 1H), consistent with the sex-dependent significant increases in lean mass. Further analyses of femoral bone, using three-dimensional high resolution micro-computed tomography (μCT), confirmed an astonishing increase in trabecular bone mass and microarchitecture in older *Esr1*$^{Nkx2\text{-}1Cre}$ females compared to control littermates (Fig 2A). Mutant females exhibited a ~500% increase in fractional bone volume in the distal femur, rising from 11 to 52 BV/TV (%) (Fig 2A). A similar trend was found for vertebral bone (Supplementary Fig 3A).

Accompanying structural changes included increases in trabecular number and thickness and reduced trabecular separation (Fig 2A). Mutant females also exhibited a significant increase in cortical thickness but a modest decrease in tibial and femoral length (Supplementary Fig 3B). This striking skeletal phenotype is sex-dependent, as no changes in bone mass were observed in *Esr1*$^{Nkx2\text{-}1Cre}$ males (Fig 2B). Further, unlike the 20% increase in femoral bone mass reported for *Esr1*$^{POMC\text{-}Cre}$ and *Esr1*$^{Nestin\text{-}Cre}$ female mice that vanishes after ovariectomy, bone parameters in *Esr1*$^{Nkx2\text{-}1Cre}$ females remained elevated 5 wks following ovariectomy (OVX) (Fig 2C), implying that the bone phenotype in *Esr1*$^{Nkx2\text{-}1Cre}$ females is uncoupled from compensatory changes in ovarian steroids. In fact, no significant changes in serum E2 or T were detected in 4-5 wks old mutant females when the high bone mass phenotype is clearly present (Fig 2D-E, G).

The dense skeletal phenotype in *Esr1*$^{Nkx2\text{-}1Cre}$ females observed in femoral and vertebral trabecular bone emerged early and continued to persist in older females (52-56 wks) (Fig 2 E, G). Representative H&E stained femoral bone sections from juvenile female mice illustrate the striking increase in bone density accompanied by a marked decrease in bone marrow space (Fig 2H). Upregulation of bone metabolism in *Esr1*$^{Nkx2\text{-}1Cre}$ females was not associated with ectopic *Cre* expression in femoral bone (Supplementary Fig 3C). Mechanical bone strength tests established that femora and L5 vertebrae in older *Esr1*$^{Nkx2\text{-}1Cre}$ females were substantially stronger than controls (Fig 2F). Thus, trabecular bone, which becomes porous and more fragile in osteoporosis, is remarkably dense and durable in older *Esr1*$^{Nkx2\text{-}1Cre}$ females.

Young *Esr1*$^{Nkx2\text{-}1Cre}$ females showed a significant increase in bone formation rate (BFR) and mineralized surface (Fig 3A, B), demonstrating robust osteoblast function. Both the mineral apposition rate (MAR) and normalized osteoclast number were unaffected in mutant bone, implying that significant decreases in osteoclast number and function are

unable to account for the high bone mass phenotype (Fig 3B and Supplementary Fig 3D). A similar trend was observed in older *Esr1*$^{Nkx2\text{-}1Cre}$ females after maximal bone density is achieved (Supplementary Fig 3D). Multiple markers associated with differentiating and mature osteoblasts, including *Sp7* (*Osterix*), *Wnt10b*, *Bglap* (*Osteocalcin*), and *Sost*, as well as markers for osteoclasts were all elevated (Fig 3C). While *Runx2* was unchanged in mutant bone chips, this osteoblast precursor marker was increased in female bone marrow when examined at 4.5 wks of age (Fig 3C). Other markers such as *Sox9* (chondrocyte differentiation (23)), or *Adbr2* (adrenergic receptor signaling in bone (24, 25)) were unchanged (Supplementary Table 1). Transcriptome profiling of whole bone marrow revealed >500 differentially expressed genes in mutant females with top biological pathways (GO) suggesting upregulation of BMP signaling and osteoblast differentiation/ossification (*Sfrp2, Bmpr1a, Itga11, Bmp3, Col2a1, Cat*). Markers of Interferon signaling (*Oas2, Oas3, Itga11, Gbp6, Gbp4*) were also elevated (Fig 3D and Supplementary Fig 3E and Dataset 2), consistent with the estrogen-independent increases in bone mass following interferon-gamma treatment (26). Collectively, these data suggest an expansion of osteoblasts and/or bone marrow stromal cells fated for differentiation to osteoblasts to mature bone after ablating ERα in the MBH.

To unequivocally establish that the high bone mass phenotype in *Esr1*$^{Nkx2\text{-}1Cre}$ females arises specifically from loss of ERα signaling in the brain, stereotaxic delivery of AAV2-Cre was used to eliminate ERα in either the VMHvl or the ARC (referred to as ERαKO^{VMHvl} or ERαKO^{ARC}, respectively, Fig 4A). Adult *Esr1*$^{fl/fl}$ females injected with either AAV2-GFP (control) or AAV2-Cre were evaluated for ERα expression (Supplementary Fig 4A, B). Successful hits were defined as partial or full loss of ERα on one or both sides of the VMHvl or ARC. As noted for *Esr1*$^{Nkx2\text{-}1Cre}$ females, eliminating ERα in the ARC but not the VMHvl fully recapitulated the significant increase in BMD without changing food intake or

E2, T, Leptin, and uterine weights (Fig 4B-D and Supplementary 5A), disentangling the high bone mass phenotype in ERαKO^{ARC} females from changes in these three circulating hormones. Strikingly, just 12 wks post infection (PI), ERαKO^{ARC} females showed a similar massive elevation in fractional femoral bone volume, which was accompanied by an increase in trabecular number and thickness and decreased bone marrow space (Fig 4E-G), as well as a modest increase in osteoprotegerin (OPG) and elevated SOST (Supplementary Fig 5A). Cortical bone thickness was also enhanced without affecting the cortical perimeter (Fig 4G and Supplementary Fig 5B).

The impact of viral-mediated deletion of ERα in the ARC was assessed over time in OVX females that model post-menopausal bone loss. As expected, in vivo imaging showed that volumetric bone in OVX females dropped rapidly after ovariectomy, dipping by half from ~11 to 5.6 ± 1.3 SD %BV/TV for all cohorts. Bone mass declined further to ~3.1± 0.9 SD %BV/TV during the 5 wk post-infection period, the time required to achieve complete ERα deletion in the ARC (27). While bone density continued to deteriorate in control groups where ERα remained intact (GFP or Miss), complete or partial loss of ERα in the ARC (Hits) resulted in a remarkable ~50% increase in bone volume 12 wks post-infection despite the mature age (38 wks) of these older females (Fig 4G and Supplementary Fig 4C). In sum, these data using both intact and older estrogen-depleted females suggest that the increased bone formation observed in *Esr1*$^{Nkx2\text{-}1Cre}$ females is central in origin, thus supporting the existence of a robust estrogen-sensitive neuroskeletal circuit.

To assess molecular changes in the ARC that are associated with upregulation of bone metabolism in *Esr1*$^{Nkx2\text{-}1Cre}$ females, transcriptional profiling was performed. Using microdissected female ARC tissue from controls and mutants, we defined ~180 differentially expressed genes (DEG) significantly changed in *Esr1*$^{Nkx2\text{-}1Cre}$ mutants (Fig 5A, B). Of those transcripts, 83% overlapped with genes that are known to be regulated by estrogen (Fig 5C)

as illustrated by loss of *Greb1*, a highly responsive ERα gene target(28). Strikingly, however, more than 100 differentially regulated transcripts were distinct from the well-characterized markers of either POMC or AgRP neurons (Fig 5C and Supplementary Dataset 1). Among significantly downregulated genes, four transcripts are associated with dopaminergic neurons: the dopamine transporter *Slc6a3* (DAT), the synaptic vesicle glycoprotein *Sv2c*, the transcription factor *Nr4a2*, and the prolactin receptor *Prlr* (Fig 5A). After loss of ERα, *Slc6a3* is downregulated in the ARC consistent with *Slc6a3* upregulation by E2 in cultured cells(29) (Fig 5A, D-E). Interestingly, circulating prolactin levels, which are normally restrained by hypothalamic dopamine and *Prlr* (30), are elevated in mutant females (Supplementary Fig 5C). Accordingly, we find that the majority of DAT-positive neurons in the dorsal medial ARC coexpress ERα, by means of an *Slc6a3*$^{Cre;Tdtomato}$ reporter line (Fig 5E). Another triad of DEGs is *Kiss1*, *Pdyn*, and *Tac2* (Fig 5B, D) that together with the glutamate transporter *Slc17a6* define KNDy (Kisspeptin, Neurokinin B, Dynorphin) ARC neurons (31, 32). As expected and based on the dynamic transcriptional repression of KNDy markers by estrogen (33, 34), both *Kiss1* and *Pdyn* are elevated in *Esr1*$^{Nkx2\text{-}1Cre}$ mutants.

Given that the gene signature of KNDy neurons is altered in *Esr1*$^{Nkx2\text{-}1Cre}$ females, we then deleted ERα in *Kiss1* cells (*Esr1*$^{Kiss1\text{-}Cre}$) using a *Kiss1-Cre-GFP* knockin allele to ask if we might identify which estrogen-responsive ARC neurons drive the robust female bone phenotype. As the majority of *Kiss1* neurons share a common lineage with *POMC* neurons in development (34), we also deleted ERα in *POMC* neurons (*Esr1*$^{POMC\text{-}Cre}$). While ERα was partially ablated in the *Esr1*$^{POMC\text{-}Cre}$ ARC, we failed to detect a trabecular or cortical bone phenotype previously reported for *Esr1*$^{POMC\text{-}Cre}$ females (1) (Fig 6A and Supplementary Fig 6A); our negative results could stem from strain, dosage or transmission (paternal vs maternal) differences. In stark contrast, after confirming loss of ERα in all *Kiss1* ARC neurons in *Esr1*$^{Kiss1\text{-}Cre}$ females (Fig 6B and Supplementary Fig 6B, C), both juvenile and

older mutant females displayed a stunning increase in bone mass that was easily visualized by the naked eye (Fig 6C), with values reaching 88%BV/TV for the distal femur; mutant L5 vertebrae and cortical bone mass were similarly affected (Fig 6D). The striking elevation in bone density in *Esr1*$^{Kiss1\text{-}Cre}$ females exceeded the observed bone mass in *Esr1*$^{Nkx2\text{-}1Cre}$ females at all ages. Similar to *Esr1*$^{Nkx2\text{-}1Cre}$ mice the bone phenotype is limited to females and appears to be independent of high E2 levels (Fig 6D and Supplemental Fig 6B), consistent with the findings that deleting ERα with an earlier *Kiss1-Cre* knockin allele accelerates pubertal onset in female mice without altering negative feedback (16, 35). Although we observed similar E2 levels in *Esr1*$^{Kiss1\text{-}Cre}$ at 4.5-19 wks, the premature LH surge (and E2) in juvenile females noted by others using *Kiss1-Cre*s (16, 36) could account for the higher volumetric bone mass observed in *Esr1*$^{Kiss1\text{-}Cre}$ versus *Esr1*$^{Nkx2\text{-}1Cre}$ females (79 ± 4.8 vs 52 ± 4.5 %BV/TV distal femurs). As might be predicted with extremely dense bone and probable bone marrow failure, spleen weights increase significantly in young and older females (Fig 6D). Taken together, the contrasting bone phenotypes observed in *Esr1*$^{Kiss1\text{-}Cre}$ and *Esr1*$^{POMC\text{-}Cre}$ infer that this female-specific brain-to-bone pathway is mediated by a subset of *Kiss1* neurons independent of other ARC neuronal progenitors such as POMC (34). Collectively, our data also suggest that disrupting the transcriptional output and activity of KNDy neurons breaks a brain-bone homeostatic axis that would normally restrain anabolic bone metabolism.

Discussion

Our investigation to understand the complex role of estrogen signaling in the MBH established that ERα-expressing *Kiss1* ARC neurons are central to restraining a powerful brain-bone axis. This assertion stems from the sex-dependent, high bone mass phenotype that emerged from three independent, intersectional strategies that target central ERα signaling. Moreover, we find that selectively removing ERα activity in the ARC of older,

estrogen depleted females results in an impressive ~50% increase in bone density, indicating a potential therapeutic value in manipulating this female neuroskeletal circuit. When compared with other mouse models that alter bone remodeling, several prominent features emerge from our results. In particular, the only model that, to our knowledge, rivals the magnitude of volumetric bone density increase observed in *Esr1*$^{Kiss1\text{-}Cre}$ and *Esr1*$^{Nkx2\text{-}1Cre}$ females is the sclerostin null (*Sost*$^{-/-}$) mouse (37, 38). However, the *Sost*$^{-/-}$ bone phenotype is observed in both sexes and the connectivity density is substantially lower (37). Perturbation of this brain to bone axis results in a female-specific rapid alteration of bone metabolism linked to enhanced osteoblast differentiation resulting in dense, fully functional mature bone with exceptional strength. When considered alongside the well-established role of peripheral estrogen in the prevention of bone loss (39, 40), our findings imply that estrogen signaling in a subset of hypothalamic neurons dedicated to restraining the onset of puberty also inhibit anabolic bone metabolism in females. Once this ERα dependent brain-to-bone pathway is broken in females, energetic resources are funneled into bone and diverted away from reproduction and energy expenditure.

Kiss1 hypothalamic neurons can be categorized as either KNDy in the ARC or Kiss1 in the rostral ARC (AVPV). Multiple labs report that Kiss1 and KNDy subtypes are distinguished by their neuronal excitability, projections, and regulatory function of ERα, including a role of non-classical, non-ERE action (41). At this juncture, we know that deleting ERα with a *Kiss1-Cre* knock-in allele, which will target the ARC and AVPV, as well as other tissues, triggers an incredibly robust female high bone mass phenotype. When coupled with a similar phenotype observed in ERαKO^{ARC}, and the residual ERα expression in the AVPV of *Esr1*$^{Nkx2\text{-}1Cre}$ females, we reason that it is not Kiss1 AVPV neurons, but KNDy ARC neurons that regulate this sex-dependent brain-to-bone connection. Whether there are functionally distinct KNDy ARC neuronal subpopulations critical for this brain-to-bone

pathway remains to be determined. Given that prodynorphin, a marker of KNDy ARC neurons is suppressed by estrogen, but not by tamoxifen(42), one might speculate that the bone-sparing effects of this selective ERα modulator (43) stem from its antagonist activity in the ARC.

The precise neuronal or humoral signals that promote the high mass bone phenotype in *Esr1*$^{Nkx2\text{-}1Cre}$, *Esr1*$^{Kiss1\text{-}Cre}$ and ERαKO^{ARC} females remain to be determined. However, we note that this phenotype is independent of changes to leptin or E2 and is not directly influenced by ERα neurons in the VMH. In this respect, our results differ from prior reports linking leptin deficiency to high trabecular bone mass (44) via a circuit involving suppression of serotonergic signaling in the VMH (45) or direct effects of leptin on bone (46). Moreover, while lower sympathetic output in the MBH can lead to mild increases in cortical and trabecular bone over months (25), the high bone density phenotype in *Esr1*$^{Nkx2\text{-}1Cre}$ and *Esr1*$^{Kiss1\text{-}Cre}$ females arises as early as 4 wks, and all measured parameters of sympathetic tone (e.g., circulating ACTH and catecholamines, BAT *Ucp1*, and bone *Adbr2*) are not significantly different in mutant females (Supplementary Fig 3D, E and Supplementary Table 1). Importantly, the elevated bone mass in mutant females does not appear to be caused from a change in bone resorption as no change in TRAP staining was observed in mutant female femoral bone. That sclerostin, a known repressor of bone metabolism is elevated in *Esr1*$^{Nkx2\text{-}1Cre}$ mutants implies that their massive increase in female volumetric bone mass is independent of sclerostin, thus potentially representing a new undefined molecular signaling pathway that promotes bone formation.

Our findings raise an interesting question: why have a female-specific ERα brain-bone pathway that counteracts the positive effects of peripheral estrogen on bone remodeling? One clue is provided by the global role of ERα signaling in the MBH, which is to allocate energetic resources to initiate and preserve reproduction. Based on our loss-of-

function studies, we conclude that ERα signaling in MBH neurons regulates energy expenditure in this way, by promoting locomotion, generating heat via adaptive BAT thermogenesis, and preserving energy and calcium stores by preventing excessive bone building, without altering food intake. As such, our work defines central regulation of bone metabolism, alongside reproduction and energy balance, as a fundamental determinant of female physiology. This estrogen-sensitive neuroskeletal axis is likely to be relevant during the pre-pubertal growth spurt in humans and in late stages of pregnancy, when gonadal steroids are low or high, respectively.

In the course of our study, we also found that *Slc6a3* encoding DAT is highly responsive to estrogen and marks a subset of dorsal medial ERα ARC neurons. Although *Kiss1* neurons appear to be sufficient in mediating the central effects of ERα on bone, defining the contribution of DAT ARC neurons to this circuit awaits development of better genetic tools. Unfortunately, consistent with earlier studies showing limited efficacy of *Slc6a3-Cre* in the hypothalamus (47, 48) ERα remained intact in DAT+ ARC neurons in *Esr1* ^{Slc6a3Cre} mice (data not shown). Because dopaminergic ARC neurons are modulated by kisspeptin (49), it will be of interest to determine how these two estrogen responsive ARC modules communicate to coordinate female bone and energy metabolism before, during and after pregnancy.

In summary, our work reveals an unprecedented sex-dependent bone phenotype and provides unequivocal proof of brain-to-bone signaling (50). Furthermore, our findings demonstrate the importance of central estrogen signaling (which exists in a coregulatory system with peripheral estrogen) in the maintenance of bone homeostasis in females. Breaking this neuroskeletal homeostatic circuit in young and old females promotes bone health and provides a model for further mechanistic investigations that might eventually provide new opportunities to counteract age-related osteoporosis in both women and men.

Materials and Methods

Mice

The origin of the *Esr1*$^{fl/fl}$ allele and generation of *Esr1*$^{Nkx2\text{-}1Cre}$ mice are described in (8) and were maintained on CD-1 background mixed with 129P2, and C57BL/6. *Esr1*$^{POMC\text{-}Cre}$ and *Esr1*$^{Kiss1\text{-}Cre}$ mice were generated by crossing male mice harboring a single copy of the *Pomc-Cre* transgene (official allele: *Tg(Pomc1-cre)16Lowl/J*) or the *Kiss1-Cre-GFP* knockin allele to *Esr1*$^{fl/fl}$ females (official allele: *Esr1*^{tm1Sakh}). *Pomc-Cre* transgenic mice were obtained from C. Vaisse (UCSF). *Esr1*$^{POMC\text{-}Cre}$ mice were maintained on a mixed FVB/N, CD-1, 129P2, and C57BL/6 genetic background. The knockin *Kiss-Cre:GFP* (version 2) allele was a gift from R. Steiner and R. Palmiter (UW). *Esr1*$^{Kiss1\text{-}Cre}$ mice were maintained on a mixed CD-1, 129P2, and C57BL/6 genetic background. *Esr1*$^{fl/+}$;*Ai14*$^{fl/+}$;*Nkx2-1Cre* mice were generated by crossing *Esr1*$^{fl/+}$;*Ai14*$^{fl/fl}$ reporter females with *Esr1l*$^{fl/fl}$*; Nkx2-1Cre* males. The *Slc6a3*^{Cre}*;Ai9*$^{fl/+}$ reporter line was a gift from by R. Edwards (UCSF). Primer sequences used for genotyping can be found in (Supplementary Table S2). For assessment of bone mass in estrogen depleted OVX females, OVX females, ovariectomy was performed between 8-25 wks. Mice were maintained on a 12 h light/dark cycle with ad libitum access to food and to standard chow diet (5058; LabDiet, 4% fat). All animal procedures were performed in accordance with UCSF institutional guidelines under the Ingraham lab IACUC protocol of record.

Metabolic Analysis

Comprehensive Laboratory Animal Monitoring Systems (CLAMS) measured O2 consumption, CO2 exhalation, total movement (total beam breaks; X and Y axes), ambulatory movement (adjacent beam breaks; X and Y axes), and rearing (total beam breaks; Z axis) at 14 min intervals. Food intake for experiments done with *Esr1*$^{Nkx2\text{-}1Cre}$ mice and female ERαKO^{VMHvl} or ERαKO^{ARC} was determined via CLAMS. Mice were housed in CLAMS for 96 h; the first 24–48 h period of acclimation was not included in analyses. Each

experimental cohort VO2 measurements were standardized to lean mass. All CLAMS analyses in females were performed in intact animals. EchoMRI were used to measure body composition. Dual X-ray absorptiometry (DEXA) was used to measure bone mineral density (BMD) and bone mineral content (BMC).

RNA Isolation and qPCR

BAT was collected, cleaned of excess tissue and homogenized in TRIzol (Invitrogen). RNA was isolated using chloroform extraction. cDNA was synthesized using the Applied Biosystems High-Capacity cDNA Reverse Transcription Kit. Whole femur samples were cleaned of excess tissue, endplates removed, minced and placed in TRIzol. Bone marrow was flushed from femoral samples using 1% HBSS. RNA was isolated using chloroform extraction for all tissues. cDNA was synthesized with random hexamer primers with the Affymetrix reverse transcriptase kit (Affymetrix). qPCR expression analysis in femoral samples was performed using TaqMan probes (bone) or SYBR Green (BAT, brain, and bone marrow). Values were normalized to either *36b4, mCyclo* or *Gapdh*. Sequences for primer pairs can be found in (Supplemental Table 3).

Immunohistochemistry and Western Blotting

BAT was dissected, cleaned of excess tissue and homogenized in RIPA buffer (1% NP40/IGEPAL, 0.1% SDS, 50 mM 2M TrisHCL pH 7.5, 150 mM 5 M NaCl, 0.5% NaDOC, 1 mM EDTA pH 8.0) supplemented with cOmplete Protease Inhibitor Cocktail tablets (Roche Cat # 04693132001). Protein was extracted in RIPA buffer by leaving samples on ice and vortexing for 1 min every 5 min for a total of 30 min followed by centrifugation at 14,000 rcf at 4°C for 10 minutes. Protein concentration was measured using BCA Protein Assay Kit (Pierce Cat # 23225). 20 µg of protein was run on a 12% Bis-Tris gel in MOPS buffer and was blotted for either anti-UCP1 (Abcam cat # ab10983) or anti Beta actin (Cell signaling cat# 5125S). Immunohistochemistry was performed on cryosections (20 µm) collected from brains fixed in 4% paraformaldehyde using standard procedures. ERα staining used rabbit

polyclonal anti-ERα antibody (Santa Cruz Biotechnology, Dallas, TX) or rabbit polyclonal ERα antibody (EMD Millipore, Billerica, MA) or mouse monoclonal ERα antibody (Abcam, Cambridge) at a dilution of 1:1000 or 1:100, respectively. GFP staining used anti-GFP antibody (Novus Biologicals, Littleton, CO) at 1:2500. Kisspeptin staining used rabbit polyclonal anti-KISS1 at a dilution of 1:200 (Abcam, Cambridge). Confocal images were taken using a Nikon Ti inverted fluorescence microscope with CSU-22 spinning disk confocal.

***In Situ* Hybridization**

Slc6a3 cDNA for in vitro transcription of DIG-labeled riboprobe was generated by PCR amplification (forward primer: 5-TTCCGAGAGAAACTGGCCTA-3 and reverse primer: 5-TGTGAAGAGCAGGTGTCCAG-3) from a brain mRNA library. ISH was performed on 20μm sections using standard protocols (51). The DIG-riboprobe was hybridized overnight at 65°C. Following washing and blocking, sections were incubated overnight with anti-DIG-AP (1:2000) (Roche) at 4°C. AP signal was developed using BM Purple (Roche).

Serum measurements

For measurements of E2 or T, nonpolar metabolites from plasma were extracted in 1 ml of PBS with inclusion of internal standards C12:0 monoalkylglycerol ether (MAGE) (10 nmol, Santa Cruz Biotechnology) and pentadecanoic acid (10 nmol, Sigma-Aldrich) and 3 ml of 2:1 chloroform:methanol. Aqueous and organic layers were separated by centrifugation at 1000 x g for 5 min and the organic layer was collected, dried under a stream of N2 and dissolved in 120 ml chloroform. A 10uL aliquot was injected onto LC/MS and metabolites were separated by liquid chromatography as previously described (52). MS analysis was performed with an electrospray ionization (ESI) source on an Agilent 6430 QQQ LC-MS/MS (Agilent Technologies) with the fragmentor voltage set to 100 V, the capillary voltage was set to 3.0 kV, the drying gas temperature was 350°C, the drying gas flow rate was 10 l/min, and the nebulizer pressure was 35 psi. Metabolites were identified by SRM of the transition

from precursor to product ions at associated optimized collision energies and retention times as previously described (52).Metabolites were quantified by integrating the area under the curve, then normalized to internal standard values and values determined by comparison to a standard curve of each metabolite of interest run simultaneous to the experimental samples.

Plasma leptin was measured using the mouse Leptin Elisa Kit (Chrystal Chem). Circulating pituitary hormones, bone markers and plasma catecholamines were measured by the VUMC Hormone Assay and Analytic Services Core. Briefly, levels of serum pituitary hormones were measured by radioimmunoassay (RIA). Bone markers were measured by the Millipore bone metabolism mulitplex fluorescent Luminex Assay. For catecholamine analysis, plasma was collected in the afternoon and immediately treated with EGTA-glutathione and subsequently measured by HPLC.

Histology

Tissue was collected and cleaned of excess tissue and fixed in 4% paraformaldehyde and embedded in paraffin. For both BAT and ovary 5 µm sections were cut, processed, stained with hematoxylin and eosin (H&E) and bright field images were taken using the Luminera Infinity-3. Femoral samples were cleaned of soft tissue, fixed in 4% PFA and demineralized in 10% EDTA for 10-14 days before being embedded in paraffin wax. 5 µm sections were then cut using the Leica RM2165 and subsequently stained with H&E or stained with tartrate-resistant acid phosphatase (TRAP). Photoshop software was used to remove background in non-tissue areas for images taken of ovaries and distal femurs.

Stereotaxic Delivery of AAV2

Adeno-associated virus sereotype 2 (AAV2) from UNC Vector Core was injected bilaterally into isoflurane-anesthetized 9-16 wks old adult *Esr1*$^{fl/fl}$ female mice. VMH coordinates: A-P: -1.56 mm from Bregma; lateral: ± 0.85 mm from Bregma; D-V: -5.8 mm from the skull; ARC coordinates: A-P: -1.58 mm from Bregma; lateral ± 0.25 mm from

Bregma; D-V: -5.8 mm from the skull. AAV2-virus was injected bilaterally into adult *Esr1*$^{fl/fl}$ 19-24 wks old female mice 5-8 wks post OVX. Buprenorphine (0.1 mg/kg i.p.) was provided as analgesia after surgery and as needed. For animals receiving AAV2-Cre, an n of at least 12 was used to ensure a large enough sample size taking into account anticipated misses or miss-targeting of AAV2 virus. Misses were characterized as no ablation of ERα in the VMH or ARC in AAV2-Cre groups.

Micro Computed Tomography (µCT)

Volumetric bone density and bone volume were measured at the right femur, tibio-fibular joint, or midshaft, and L5 vertebrae using a Scanco Medical µCT 50 specimen scanner calibrated to a hydroxyapatite phantom. Briefly, samples were fixed in 10% phosphate-buffered formalin and scanned in 70% ethanol. Scanning was performed using a voxel size of 10mm and an X-ray tube potential of 55 kVp and X-ray intensity of 109 µA. Scanned regions included 2 mm region of the femur proximal to epiphyseal plate, 1 mm region of the femoral mid-diaphysis and the whole L5 vertebrae.

Longitudinal live animal µCT imaging was performed using a Scanco Medical vivaCT 40 preclinical scanner. Animals were anesthetized and a 2 mm region of the distal femur was scanned. Similarly, a trabecular bone compartment of 1mm length proximal to the epiphyseal plate was measured. Cortical parameters were assessed at the diaphysis in an adjacent 0.4 mm region of the femur.

In both specimen and in vivo scanning, volumes of interest were evaluated using Scanco evaluation software. Representative 3D images created using Scanco Medical mCT Ray v4.0 software. Segmented volume of trabecular bone presented from anterior perspective and ventral side of vertebrae. Segmented volume of cortical bone presented as transverse cross-sectional image.

Biomechanical Strength Tests

Right femurs underwent three-point bend test using the ElectroForce 3200 mechanical load frame. Lower supports were separated by a span of 8 mm to support two ends of the specimen. The testing head was aligned at the midpoint between the supports. Femurs were preloaded to a force of 1N then loaded at a rate of 0.2 mm/s. Loading was terminated upon mechanical failure, determined by a drop in force to 0.5 N. Force displacement data collected every 0.01s. Load-to-failure tests were performed to measure the uniaxial compressive strength of the L5 vertebral bodies. Before testing, the posterior elements and endplates were removed from the vertebrae, resulting in vertebral bodies with plano-parallel ends. Tests included five preconditioning cycles to 0.3% strain followed by a ramp to failure at a rate of 0.5% strain/sec. Vertebral strength was defined as the maximum compressive force sustained during the tests. All tests were performed at room temperature using an electro-mechanical load frame (Electroforce 3200; Bose, Eden Prairie, MN).

Dynamic Histomorphometry

To determine bone formation and mineralization, females (age 12-14 and 33 wks) were injected with 20 mg/kg of calcein (Sigma-Aldrich, St Louis, MO, USA) 7 days before euthanasia along with 15 mg/kg of demeclocycline (Sigma-Aldrich) 2 days before euthanasia. Bones were fixed in 4% formalin. Before histomorphometric analysis, mosaic-tiled images of distal femurs were acquired at x20 magnification with a Zeiss Axioplan Imager M1 microscope (Carl Zeiss MicroImaging) fitted with a motorized stage. The tiled images were stitched and converted to a single image using the Axiovision software (Carl Zeiss MicroImaGing) prior to blinded analyses being performed using image-analysis software (Bioquant Image Analysis Corp., Nashville, TN, USA). The dynamic indices of bone formation within the same region that were measured on 10-mm sections and percent mineralizing surface (MS/BS), mineral apposition rate (MAR), and surface-based bone-formation rate (BFR/BS) were determined by Bioquant OSTEO software.

Microdissection and Transcriptional Profiling of the ARC and Bone Marrow

Flushed bone marrow was obtained as described above from control and mutant female femur at 4.5 wks of age. Microdissected ARC tissue was obtained from control and mutant female mice (11-20 wks old) using the optic chiasm as a reference point, a 2 mm block of tissue containing the hypothalamus was isolated with a matrix slicer. Microdissection techniques were validated by enrichment for *AgRP*, *Cited* 1 (ARC) and absence of *Tac1*, *Cbln1* (VMH). For both bone marrow and ARC, total RNA was purified using the PureLink RNA Mini Kit (Invitrogen, Waltham MA). Amplified cDNA was generated from 10-50 ng of total RNA using the Ovation RNA-Seq System V2 or Trio (Nugen, San Carlos, CA). For the ARC, cDNA was fragmented to 200 bp using a Covaris M220 sonicator (Covaris, Woburn, MA). For the ARC, barcoded sequencing libraries were prepared from 100 ng of fragmented cDNA using the Ovation Ultralow System V2 (Nugen, San Carlos, CA) and single-end 50 bp reads sequenced from the multiplexed libraries on the HiSeq 4000 (Illumina, San Diego, CA) at the UCSF Center for Advanced Technologies. For ARC and bone marrow samples, sequencing generated reads were mapped to the mouse genome (NCBI37/mm10) using TopHat2. Reads that mapped to exons in annotated genes were counted using HTSeq (53). Final quantification and statistical testing of differentially expressed genes (adjusted p-value < 0.05) was performed using DESeq2 (54).

Acknowledgements:

We wish to thank Drs. A. Bertholet, R. Edwards, S. Khan, E. Hsiao, C. Paillart, Y. Lin, R. Steiner, R. Palmiter, A. Xu and C. Vaisse for reagents, discussions and C. Cain and A. Matcham for assistance with data acquisition, Hazel A. Escusa and James Bayrer for assistance and also M. Horwitz at the Gladstone Institute Histology Core. This research was supported by grants to H.A.I (R01 DK099722, and NRSA NDSP P30-DK097748), S.M.C (K01 DK098320 and UCLA Women's Health Center and CTSI (NIH UL1TR001881), C.B.H (F32 DK107115-01A1 and AHA Postdoctoral Fellowship 16POST29870011), W.C.K (AHA Postdoctoral Fellowship 16POST27260361), R.A.N (VA Merit Review Grant 1I01BX003212), C.C (NIH T32 DK007161), A. F (NIH P30 AR066262) and D.K.N (NIH/NCI R01CA172667). We acknowledge the UCSF DERC (NIDDK P30 DK063720), the UCSF CCMBM (NIH P30 AR066262) and the Vanderbilt Hormone Assay Core (NIH DK059637 and DK020593).

Author contributions:

C.B.H. and W.C.K. designed experiments, analyzed data and wrote the paper. B.F. performed mass spectrometry analysis of mouse serum. L.W. performed histomorphometric and data analyses. J.R.B. performed immunohistochemistry and imaging on coronal brain sections. A.L. performed microCT, 3-point bend test and tissue embedding of femurs. M.S.R. performed immunohistochemistry and subsequent imaging on coronal brain sections. A.F. performed L5 vertebral crush test. M.S. performed RNA-seq analysis on bone marrow. D.K.N. provided expertise in mass spectrometry metabolic analysis. R.A.N helped design experiments and provided expertise in bone biology. S.M.C. designed experiments, provided animal models and analyzed data. H.A.I designed experiments and wrote the paper.

References:

1. Farman HH*, et al.* (2016) Female Mice Lacking Estrogen Receptor-alpha in Hypothalamic Proopiomelanocortin (POMC) Neurons Display Enhanced Estrogenic Response on Cortical Bone Mass. Endocrinology 157(8):3242-3252.
2. Perry MJ, Gujra S, Whitworth T, & Tobias JH (2005) Tamoxifen stimulates cancellous bone formation in long bones of female mice. Endocrinology 146(3):1060-1065.
3. Ohlsson C*, et al.* (2012) Estrogen receptor-alpha expression in neuronal cells affects bone mass. Proc Natl Acad Sci U S A 109(3):983-988.
4. Harno E, Cottrell EC, & White A (2013) Metabolic pitfalls of CNS Cre-based technology. Cell Metab 18(1):21-28.
5. Padilla SL, Reef D, & Zeltser LM (2012) Defining POMC neurons using transgenic reagents: impact of transient Pomc expression in diverse immature neuronal populations. Endocrinology 153(3):1219-1231.
6. Baldock PA*, et al.* (2002) Hypothalamic Y2 receptors regulate bone formation. J Clin Invest 109(7):915-921.
7. Kim JG*, et al.* (2015) AgRP Neurons Regulate Bone Mass. Cell Rep 13(1):8-14.
8. Correa SM*, et al.* (2015) An estrogen-responsive module in the ventromedial hypothalamus selectively drives sex-specific activity in females. Cell Rep 10(1):62-74.
9. Xu Y*, et al.* (2011) Distinct hypothalamic neurons mediate estrogenic effects on energy homeostasis and reproduction. Cell Metab 14(4):453-465.
10. Krause WC & Ingraham HA (2017) Origins and Functions of the Ventrolateral VMH: A Complex Neuronal Cluster Orchestrating Sex Differences in Metabolism and Behavior. Adv Exp Med Biol 1043:199-213.
11. Martinez de Morentin PB*, et al.* (2014) Estradiol regulates brown adipose tissue thermogenesis via hypothalamic AMPK. Cell Metab 20(1):41-53.
12. de Souza FS*, et al.* (2011) The estrogen receptor alpha colocalizes with proopiomelanocortin in hypothalamic neurons and binds to a conserved motif present in the neuron-specific enhancer nPE2. Eur J Pharmacol 660(1):181-187.
13. Han SK*, et al.* (2005) Activation of gonadotropin-releasing hormone neurons by kisspeptin as a neuroendocrine switch for the onset of puberty. J Neurosci 25(49):11349-11356.
14. d'Anglemont de Tassigny X*, et al.* (2007) Hypogonadotropic hypogonadism in mice lacking a functional Kiss1 gene. Proc Natl Acad Sci U S A 104(25):10714-10719.
15. Topaloglu AK*, et al.* (2012) Inactivating KISS1 mutation and hypogonadotropic hypogonadism. N Engl J Med 366(7):629-635.
16. Mayer C*, et al.* (2010) Timing and completion of puberty in female mice depend on estrogen receptor alpha-signaling in kisspeptin neurons. Proc Natl Acad Sci U S A 107(52):22693-22698.
17. Frazao R*, et al.* (2013) Shift in Kiss1 cell activity requires estrogen receptor alpha. J Neurosci 33(7):2807-2820.

18. Dubois SL, Wolfe A, Radovick S, Boehm U, & Levine JE (2016) Estradiol Restrains Prepubertal Gonadotropin Secretion in Female Mice via Activation of ERalpha in Kisspeptin Neurons. Endocrinology 157(4):1546-1554.
19. Olofsson LE, Pierce AA, & Xu AW (2009) Functional requirement of AgRP and NPY neurons in ovarian cycle-dependent regulation of food intake. Proc Natl Acad Sci U S A 106(37):15932-15937.
20. Padilla SL*, et al.* (2017) AgRP to Kiss1 neuron signaling links nutritional state and fertility. Proc Natl Acad Sci U S A 114(9):2413-2418.
21. Zhang X & van den Pol AN (2016) Hypothalamic arcuate nucleus tyrosine hydroxylase neurons play orexigenic role in energy homeostasis. Nat Neurosci 19(10):1341-1347.
22. Antonson P*, et al.* (2014) aP2-Cre-mediated inactivation of estrogen receptor alpha causes hydrometra. PLoS One 9(1):e85581.
23. Akiyama H, Chaboissier MC, Martin JF, Schedl A, & de Crombrugghe B (2002) The transcription factor Sox9 has essential roles in successive steps of the chondrocyte differentiation pathway and is required for expression of Sox5 and Sox6. Genes Dev 16(21):2813-2828.
24. Kondo H & Togari A (2011) Continuous treatment with a low-dose beta-agonist reduces bone mass by increasing bone resorption without suppressing bone formation. Calcif Tissue Int 88(1):23-32.
25. Takeda S*, et al.* (2002) Leptin regulates bone formation via the sympathetic nervous system. Cell 111(3):305-317.
26. Duque G*, et al.* (2011) Interferon-gamma plays a role in bone formation in vivo and rescues osteoporosis in ovariectomized mice. J Bone Miner Res 26(7):1472-1483.
27. Yeo SH & Herbison AE (2014) Estrogen-negative feedback and estrous cyclicity are critically dependent upon estrogen receptor-alpha expression in the arcuate nucleus of adult female mice. Endocrinology 155(8):2986-2995.
28. Stossi F*, et al.* (2004) Transcriptional profiling of estrogen-regulated gene expression via estrogen receptor (ER) alpha or ERbeta in human osteosarcoma cells: distinct and common target genes for these receptors. Endocrinology 145(7):3473-3486.
29. Eghlidi DH & Urbanski HF (2015) Effects of Age and Estradiol on Gene Expression in the Rhesus Macaque Hypothalamus. Neuroendocrinology 101(3):236-245.
30. Brown RS*, et al.* (2016) Conditional Deletion of the Prolactin Receptor Reveals Functional Subpopulations of Dopamine Neurons in the Arcuate Nucleus of the Hypothalamus. J Neurosci 36(35):9173-9185.
31. Goodman RL*, et al.* (2007) Kisspeptin neurons in the arcuate nucleus of the ewe express both dynorphin A and neurokinin B. Endocrinology 148(12):5752-5760.
32. Campbell JN*, et al.* (2017) A molecular census of arcuate hypothalamus and median eminence cell types. Nat Neurosci 20(3):484-496.
33. Smith JT, Cunningham MJ, Rissman EF, Clifton DK, & Steiner RA (2005) Regulation of Kiss1 gene expression in the brain of the female mouse. Endocrinology 146(9):3686-3692.
34. Sanz E*, et al.* (2015) Fertility-regulating Kiss1 neurons arise from hypothalamic POMC-expressing progenitors. J Neurosci 35(14):5549-5556.

35. Dubois SL*, et al.* (2015) Positive, but not negative feedback actions of estradiol in adult female mice require estrogen receptor alpha in kisspeptin neurons. Endocrinology 156(3):1111-1120.

36. Greenwald-Yarnell ML*, et al.* (2016) ERalpha in Tac2 Neurons Regulates Puberty Onset in Female Mice. Endocrinology 157(4):1555-1565.

37. Collette NM*, et al.* (2012) Targeted deletion of Sost distal enhancer increases bone formation and bone mass. Proc Natl Acad Sci U S A 109(35):14092-14097.

38. Li X*, et al.* (2008) Targeted deletion of the sclerostin gene in mice results in increased bone formation and bone strength. J Bone Miner Res 23(6):860-869.

39. Krum SA*, et al.* (2008) Estrogen protects bone by inducing Fas ligand in osteoblasts to regulate osteoclast survival. EMBO J 27(3):535-545.

40. Riggs BL, Khosla S, & Melton LJ, 3rd (1998) A unitary model for involutional osteoporosis: estrogen deficiency causes both type I and type II osteoporosis in postmenopausal women and contributes to bone loss in aging men. J Bone Miner Res 13(5):763-773.

41. Glidewell-Kenney C*, et al.* (2007) Nonclassical estrogen receptor alpha signaling mediates negative feedback in the female mouse reproductive axis. Proc Natl Acad Sci U S A 104(19):8173-8177.

42. Spampinato S, Canossa M, Campana G, Carboni L, & Bachetti T (1995) Estrogen regulation of prodynorphin gene expression in the rat adenohypophysis: effect of the antiestrogen tamoxifen. Endocrinology 136(4):1589-1594.

43. DeMaria JE, Livingstone JD, & Freeman ME (2000) Ovarian steroids influence the activity of neuroendocrine dopaminergic neurons. Brain Res 879(1-2):139-147.

44. Ducy P*, et al.* (2000) Leptin inhibits bone formation through a hypothalamic relay: a central control of bone mass. Cell 100(2):197-207.

45. Yadav VK*, et al.* (2009) A serotonin-dependent mechanism explains the leptin regulation of bone mass, appetite, and energy expenditure. Cell 138(5):976-989.

46. Turner RT*, et al.* (2013) Peripheral leptin regulates bone formation. J Bone Miner Res 28(1):22-34.

47. Doan KV*, et al.* (2016) FoxO1 in dopaminergic neurons regulates energy homeostasis and targets tyrosine hydroxylase. Nat Commun 7:12733.

48. Backman CM*, et al.* (2006) Characterization of a mouse strain expressing Cre recombinase from the 3' untranslated region of the dopamine transporter locus. Genesis 44(8):383-390.

49. Szawka RE*, et al.* (2010) Kisspeptin regulates prolactin release through hypothalamic dopaminergic neurons. Endocrinology 151(7):3247-3257.

50. Dimitri P & Rosen C (2016) The Central Nervous System and Bone Metabolism: An Evolving Story. Calcif Tissue Int.

51. Kurrasch DM*, et al.* (2007) The neonatal ventromedial hypothalamus transcriptome reveals novel markers with spatially distinct patterning. J Neurosci 27(50):13624-13634.

52. Benjamin DI*, et al.* (2013) Ether lipid generating enzyme AGPS alters the balance of structural and signaling lipids to fuel cancer pathogenicity. Proc Natl Acad Sci U S A 110(37):14912-14917.

53. Anders S, Pyl PT, & Huber W (2015) HTSeq--a Python framework to work with high-throughput sequencing data. Bioinformatics 31(2):166-169.

54. Love MI, Huber W, & Anders S (2014) Moderated estimation of fold change and dispersion for RNA-seq data with DESeq2. Genome Biol 15(12):550.

55. Csoregh L, Andersson E, & Fried G (2009) Transcriptional analysis of estrogen effects in human embryonic neurons and glial cells. Neuroendocrinology 89(2):171-186.

56. Monroe DG*, et al.* (2005) Estrogen receptor alpha and beta heterodimers exert unique effects on estrogen- and tamoxifen-dependent gene expression in human U2OS osteosarcoma cells. Mol Endocrinol 19(6):1555-1568.

57. Sternson SM, Atasoy D, Betley JN, Henry FE, & Xu S (2016) An Emerging Technology Framework for the Neurobiology of Appetite. Cell Metab 23(2):234-253.

Figures and Figure Legends

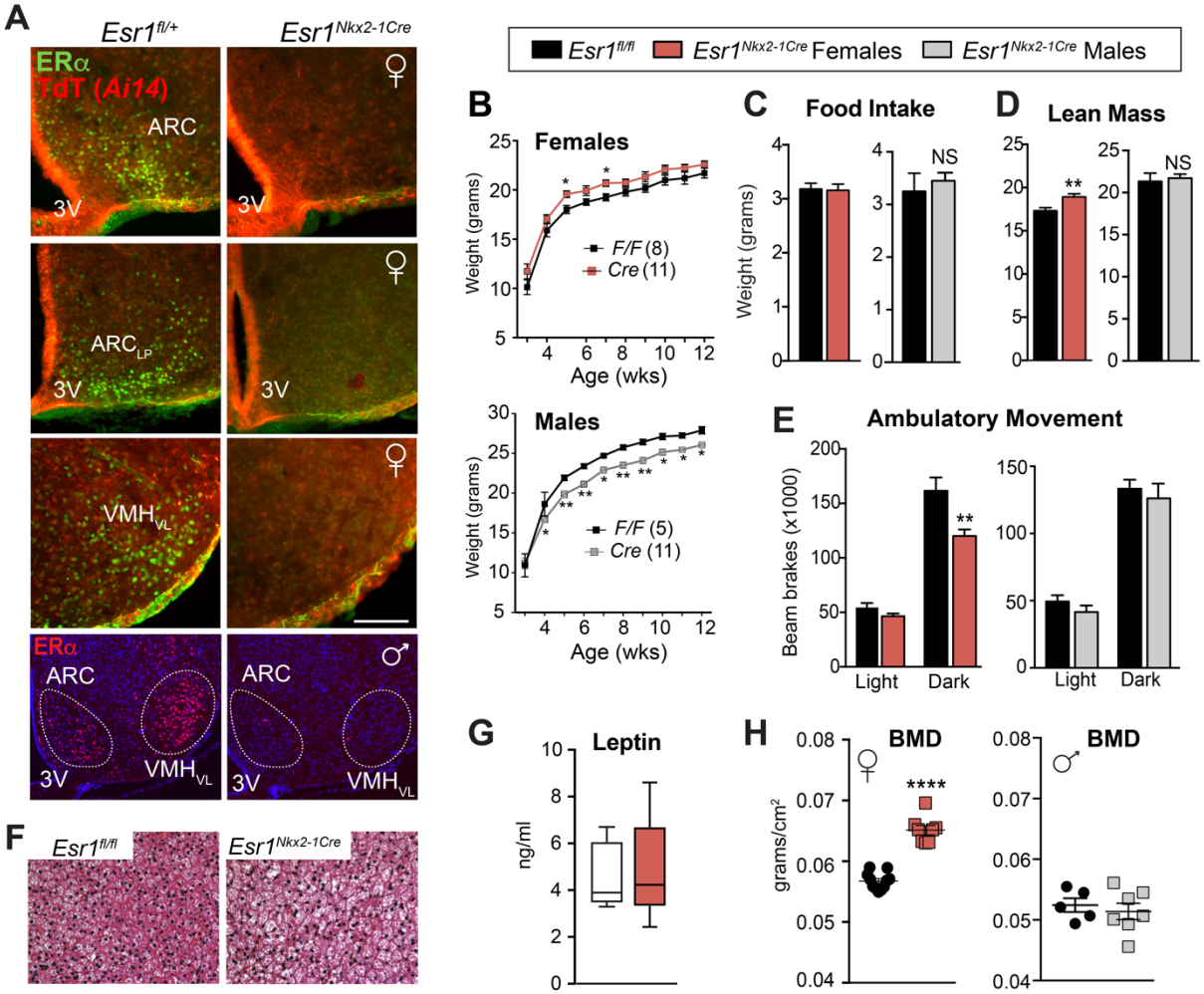

Fig. 1. Ablating ERα in the MBH impairs energy expenditure and increases bone density. (**A**) Immunohistochemistry of ERα (green) or native TdTomato (TdT (Ai14); red) on coronal brain sections (scale bar = 100 μm) of *Esr1*$^{fl/+}$; *Ai14*$^{fl/+}$; *Nkx2-1Cre* (control) or *Esr1*$^{fl/fl}$; *Ai14*$^{fl/+}$; *Nkx2-1Cre* (mutant) from females or males (bottom panels). Lp = Lateroposterior. (**B**) Body weight curves of control or mutant females ($F_{1,250}$ = 57.01, p < 0.0001) and males ($F_{3,316}$ = 25.39, p < 0.0001) fed on standard chow from 3 wks of age. (**C**) Daily food intake per animal over 24 h determined in CLAMS. (**D**) Lean mass and (**E**) averages of ambulatory movement per animal over 12 h determined by metabolic chamber analyses for *Esr1*$^{fl/fl}$ and *Esr1*$^{Nkx2-1Cre}$ female and male cohorts, female ambulatory movement (F 1,36 = 10.14, p =

0.003). (**F**) Representative images of hematoxylin and eosin (H&E) staining of BAT *Esr1*$^{fl/fl}$ and *Esr1*$^{Nkx2\text{-}1Cre}$ females housed at 22°C. (**G**) Serum leptin levels in 9 wk old control (n = 5) and mutant females (n = 5). (**H**) BMD measured by DEXA in *Esr1*$^{fl/fl}$ and *Esr1*$^{Nkx2\text{-}1Cre}$ females (16-23 wks) and males (11-18 wks). Unless otherwise indicated, number per group for female controls (n = 11) and mutants (n = 9) and for male controls (n = 4) and mutants (n = 5). Error bars ± SEM. and. Two-way ANOVA (Panels B, E) Unpaired Student's *t*-tests (Panels C, D G and H). For all figures, p values = *p < 0.05; **p < 0.01; ***p < 0.001; ****p < 0.0001. NS = p > 0.05.

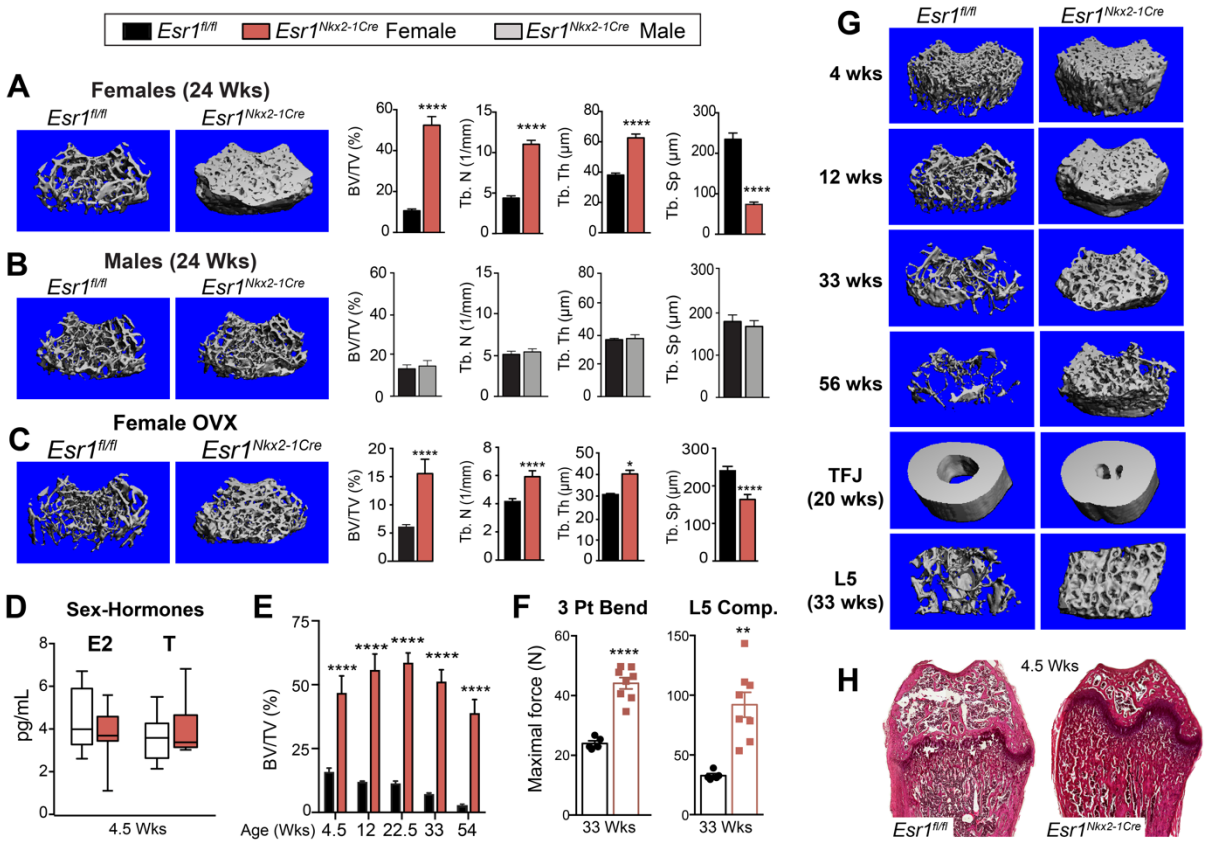

Fig. 2. Sex-dependent increase in bone mass and strength in *Esr1$^{Nkx2-1Cre}$* females. Representative µCT 3D reconstruction images of distal femurs in ~24 wk old *Esr1$^{fl/fl}$* and *Esr1$^{Nkx2-1Cre}$* (**A**) females, (**B**) males and (**C**) OVX females. Right panels show quantitative morphometric properties of distal femurs showing fractional bone volume (BV/TV (%); trabecular number (Tb. N) trabecular thickness (Tb.Th) and separation (Tb. Sp). (**D**) LC-MS/MS of plasma E2 and T for *Esr1$^{fl/fl}$* (n = 9) and *Esr1$^{Nkx2-1Cre}$* (n = 11) females at 4.5 wks of age. (**E**) BV/TV (%) of the distal femur generated by either µCT or 2D histomorphometric analysis over time from 4.5 wks of age to 54 wks of age, for genotype ($F_{1,37}$ = 147.8, p<0.0001, animal number in Materials and Methods for each age group. (**F**) Scatter plot of mechanical testing of distal femurs and L5 vertebral bodies. (**G**) Representative µCT images of age-dependent changes in femoral bone mass, as well as image of cortical bone at the tibial fibular joint (TFJ) in females (20 wks), and L5 vertebral bodies (33 wks) in *Esr1$^{fl/fl}$* and

Esr1$^{Nkx2\text{-}1Cre}$ females. (**H**) Representative H&E staining of female femurs from *Esr1*$^{fl/fl}$ and *Esr1*$^{Nkx2\text{-}1Cre}$ females at 4.5 wks. Error bars ± SEM. Two-way ANOVA (Panel E), Unpaired Student's *t*-test (Panels A-D, F).

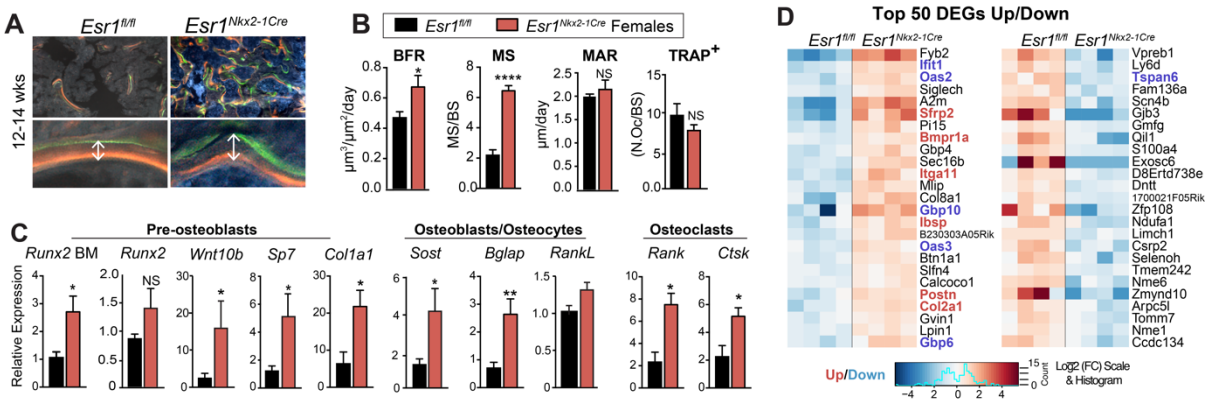

Fig. 3. Increased bone formation in *Esr1$^{Nkx2-1Cre}$* females. (**A**) Representative images of labeled mineralized surface of distal femur with calcein (green) and demeclocycline (orange) over a period of 1 wk in a 12 wk old female. (**B**) Dynamic histomorphometric results for *Esr1$^{fl/fl}$* (n = 4) and *Esr1$^{Nkx2-1Cre}$* (n = 4) 12-14 wk females showing bone formation rate (BFR), mineralized surface (MS), mineralized apposition rate (MAR). Number of active osteoclasts normalized to bone surface quantified by TRAP-positive staining determined in distal femurs from 5-7 wk old *Esr1$^{fl/fl}$* (n = 5) and *Esr1$^{Nkx2-1Cre}$* (n = 6) females. (**C**) Quantification of indicated transcripts marking pre-osteoblasts, osteocytes, and osteoclasts in 4.5-7 wk female control (n = 8) and mutant (n = 5) flushed bone marrow, or in female control (n = 6) and mutant (n = (n = 4) femur bone chips. (**D**) Heat map of top 50 differentially expressed genes (DEGs) Up and Down in *Esr1$^{fl/fl}$* and *Esr1$^{Nkx2-1Cre}$* bone marrow. BMP regulated genes (red) and IFN regulated genes (blue). Error bars ± SEM. Unpaired Student's *t*-test (Panels B and C).

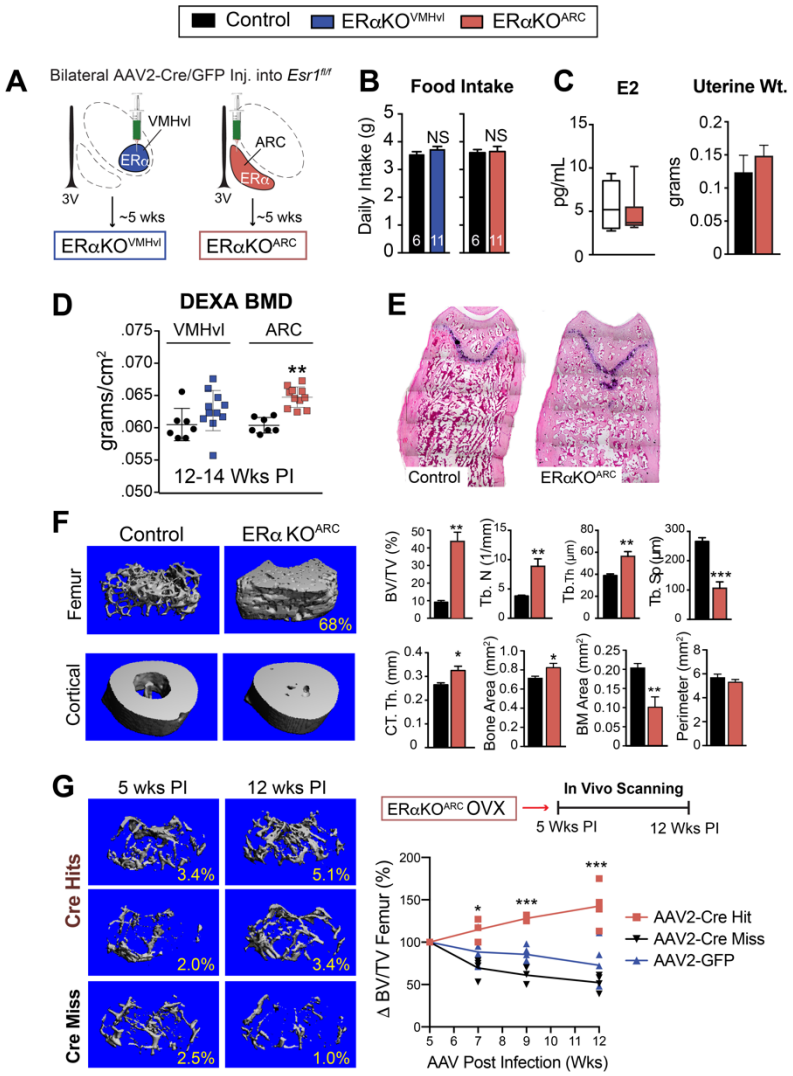

Fig. 4. Elevated bone volume in intact and estrogen depleted older female mice following acute loss of ERα in ARC. (**A**) Schematic of stereotaxic delivery of AAV2-GFP or AAV2-Cre-GFP to *Esr1*$^{fl/fl}$ females to either the VMHvl or ARC regions to delete ERα 5 wks post infection (PI). (**B**) Food intake (**C**) LC-MS/MS plasma E2 and uterine weight for control (n =6) and for ERαKO^{ARC} (n = 9-11). (**D**) Scatter plot of BMD for controls, ERαKO^{VMHvl}, and ERαKO^{ARC} females. (**E**) Representative images of distal femur (H&E) in control and ERαKO^{ARC} females. (**F**) µCT images with morphometric properties of distal femur and tibio-fibular joint in control (n = 4) and ERαKO^{ARC} (n = 6) females. (**G**)

Representative μCT images of distal femur in OVX females 5wk and 12 wks post infection, showing AAV2-Cre hit to ARC (Cre-Hits), AAV2-Cre miss to ARC (Cre-Miss). Schematic of time line for in vivo bone imaging from 5 to 12 wks PI, with graph showing percent change in volumetric bone normalized to 5 wks PI. Cre-Hits (n = 5), Cre-Miss (n = 4) and GFP (n = 5), AAV2-Cre Hit versus GFP or Miss ($F_{2,40} = 56.9$, $p<0.0001$). Error bars ± SEM. Student's unpaired *t*-test (Panels D, F). Two-way ANOVA (Panel G).

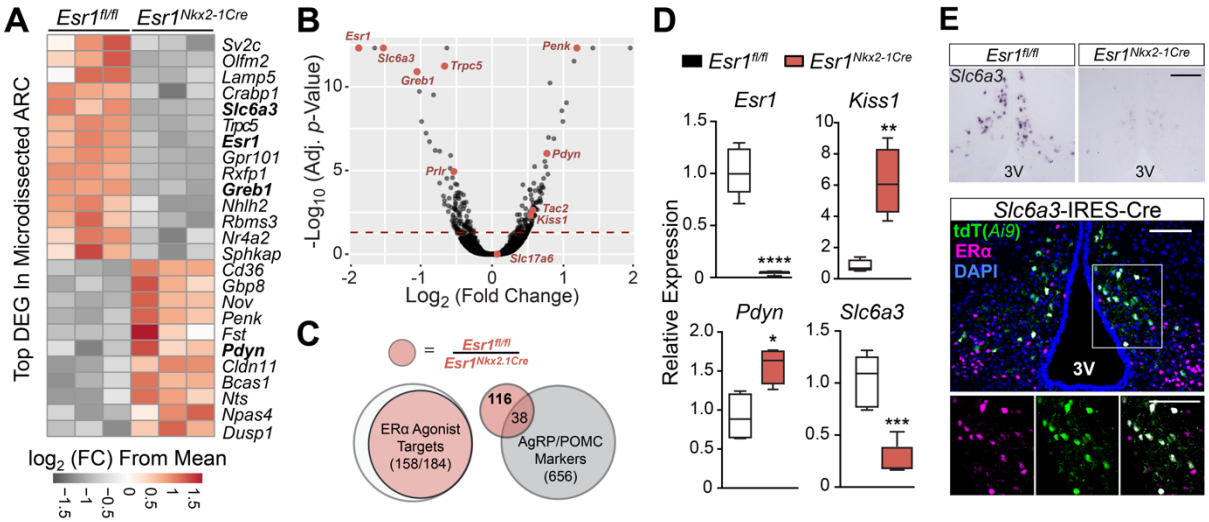

Figure 5. Increased bone formation in *Esr1*$^{Nkx2\text{-}1Cre}$ females correlates with gene changes in KNDy and DAT ARC neurons. (**A**) Heat map of top 25 most significant DEGs in ARC of *Esr1*$^{fl/fl}$ and *Esr1*$^{Nkx2.1Cre}$ females. (**B**) Volcano plot of data set with highlighted genes (red). Dashed red line represents significance cutoff with adjusted p value < 0.05). (**C**) Overlap of DEGs with adjusted *p*-value <0.05 and |log2 fold change| > 0.6 between ARC from *Esr1*$^{fl/fl}$ and *Esr1*$^{Nkx2.1Cre}$ mice (red) with identified ERα agonist-responsive transcripts (white) (55, 56) and with identified markers of AgRP and POMC neurons (grey) (57). (**D**) Expression of *Esr1*, *Kiss1*, *Pdyn,* and *Slc6a3* measured by qPCR (n = 4-6 per genotype). (**E**) ISH of *Slc6a3* in ARC and confocal image of ARC co-labeled with *Slc6a3* reporter (tdT(*Ai9*)), ERα and DAPI. Image scale bars for top and bottom panels = 100 µm.

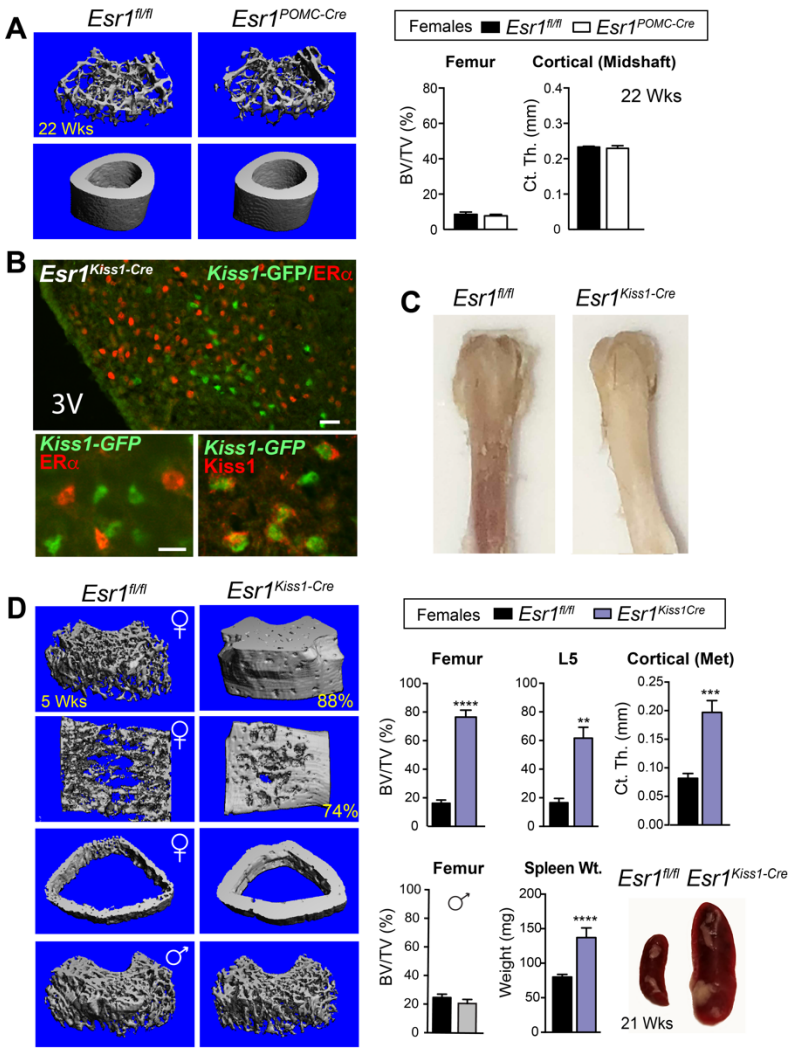

Figure 6. Conditional deletion of ERα in *Kiss1*, but not *POMC* neurons is sufficient to elicit a sex-dependent increase in bone mass. (**A**) Representative μCT images of femoral and cortical bone and quantitative BV/TV (%) and cortical thickness at midshaft of distal femur in females for *Esr1*$^{fl/fl}$ (n = 3) and *Esr1*^{PomcCre} (n = 3) at 22 wks of age. (**B**) Representative images demonstrating loss of ERα (red) in Cre-GFP-expressing *Kiss1* neurons stained for either GFP (green) or KISS1 (red) in the female ARC. Scale bars = 25 μm (top panel) and 10 μm (bottom panels) (**C**) Photograph of *Esr1*$^{fl/fl}$ and *Esr1*^{KissCre} female femurs at 6 wks of age. (**D**) μCT images of the distal femur, L5 vertebrae and cross section of cortical bone at metaphysis in *Esr1*$^{fl/fl}$ control and *Esr1*^{KissCre} mutant females as well as the

distal femur from males. %BV/TV for female distal femur controls (n = 11) and mutants (n = 4), for L5 controls (n = 6) and mutants (n = 4), and the cortical thickness at metaphysis for controls (n = 5) and mutants (n = 4). %BV/TV for male distal femur controls (n = 4) and mutants (n =4) males. Spleen weights of younger (4-5 wks) *Esr1*$^{fl/fl}$ (n = 9) and *Esr1*^{KissCre} (n = 2) and images of spleen from a control and a mutant female at 21 wks of age. Error bars ± SEM. Unpaired Student's *t*-test (Panel D).

Supplementary Information For:

Estrogen Signaling in Arcuate *Kiss1* Neurons Suppresses a Sex-Dependent Circuit That Promotes Dense Strong Bones in Female Mice

This PDF file includes:

1. Supplementary Figures

Fig. S1. *Esr1*$^{Nkx2\text{-}1Cre}$ females exhibit persistence of ERα in some brain regions and loss of fertility.

Fig. S2. Lower movement and markers of BAT in female *Esr1*$^{Nkx2\text{-}1Cre}$ mice.

Fig. S3. *Esr1*$^{Nkx2\text{-}1Cre}$ mice exhibit increased bone and BMP/Interferon signaling.

Fig. S4. Confirmation of ARC specific ablation of ERα in intact and OVX ERαKO^{ARC} females.

Fig. S5. Elevation in some cortical bone and serum factors in ERαKO^{ARC} females.

Fig. S6. Increased bone mass in *Esr1*$^{Kiss1\text{-}Cre}$ but not *Esr1*$^{Pomc\text{-}Cre}$ mice.

2. Supplemental Tables

Table S1. Gene expression in femoral bone and bone marrow in *Esr1*$^{fl/fl}$ and *Esr1*$^{Nkx2\text{-}1Cre}$ females.

Table S2. Sequences of primer pairs used for genotyping.

Table S3. Primers and probes for qPCR expression data.

3. Supplemental Data

Tab Delimited Text File of Genes changed in the ARC of *Esr1*$^{Nkx2\text{-}1Cre}$ females

Tab Delimited Text File of Genes changed in the BM of *Esr1*$^{Nkx2\text{-}1Cre}$ females

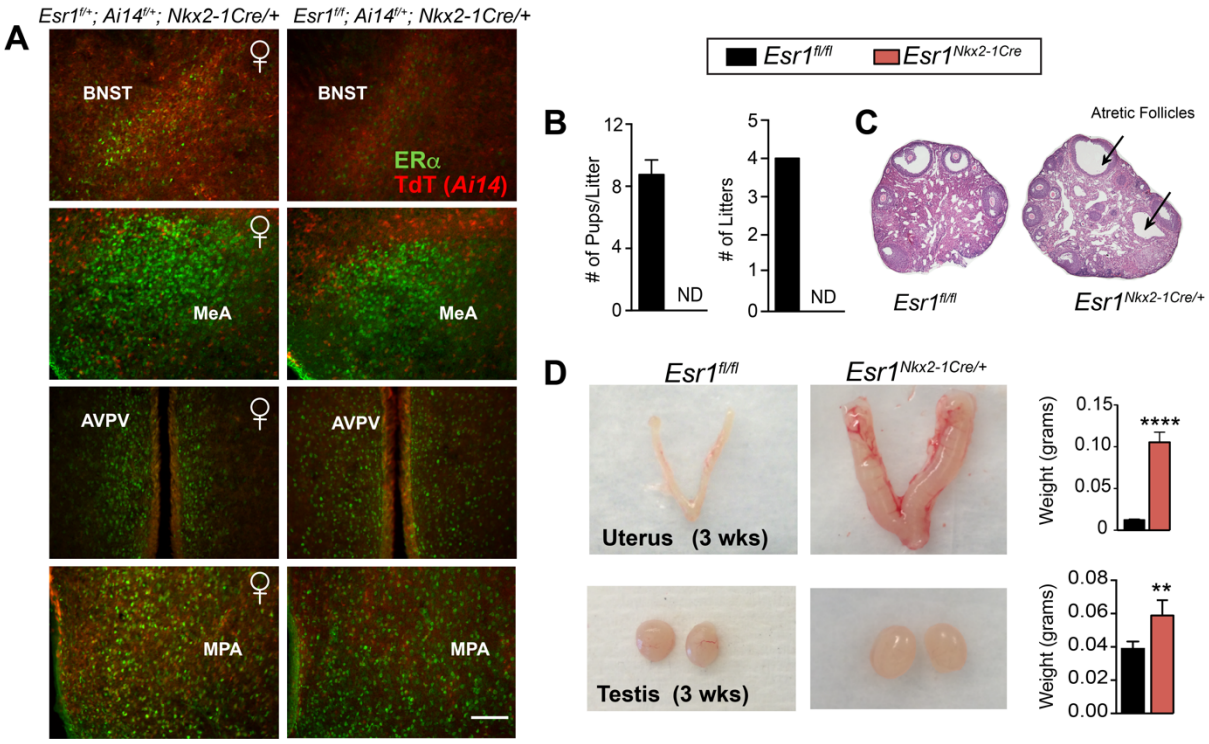

Fig. S1. *Esr1$^{Nkx2\text{-}1Cre}$* females exhibit persistence of ERα in some brain regions and loss of fertility.

(**A**) ERα immunoreactivity (green) and native TdT expression (red) in coronal brain sections of *Esr1$^{fl/+}$; Ai14$^{fl/+}$; Nkx2-1Cre* and *Esr1$^{fl/fl}$; Ai14$^{fl/+}$; Nkx2-1Cre* females. ERα expression was lost in bed nucleus of the stria terminalis (BNST) but was maintained in the medial amygdala (MeA), anteroventral periventricular nucleus (AVPV) and the medial preoptic area (MPA). Scale bar = 100µm. (**B**) Number of pups per litter and number of litters produced by mating *Esr1$^{fl/fl}$* males and females and *Esr1$^{Nkx2\text{-}1Cre}$* females with control males. ND = none detected. (**C**) Representative images of ovarian histology showing increased follicular atresia in female mutants (arrows) compared to controls. (**D**) Representative images of uteri and testis of 3 wk old *Esr1$^{fl/fl}$* and *Esr1$^{Nkx2\text{-}1Cre}$* mice with right panels showing bar graphs of uterine and testis weight of control (n = 6) and mutant (n =8) females and control (n = 6) and mutant (n =3) males at 3 wks of age. Error bars ± SEM. Statistical analysis performed was a Student's *t*-test **$p < 0.01$, ****$p < 0.0001$.

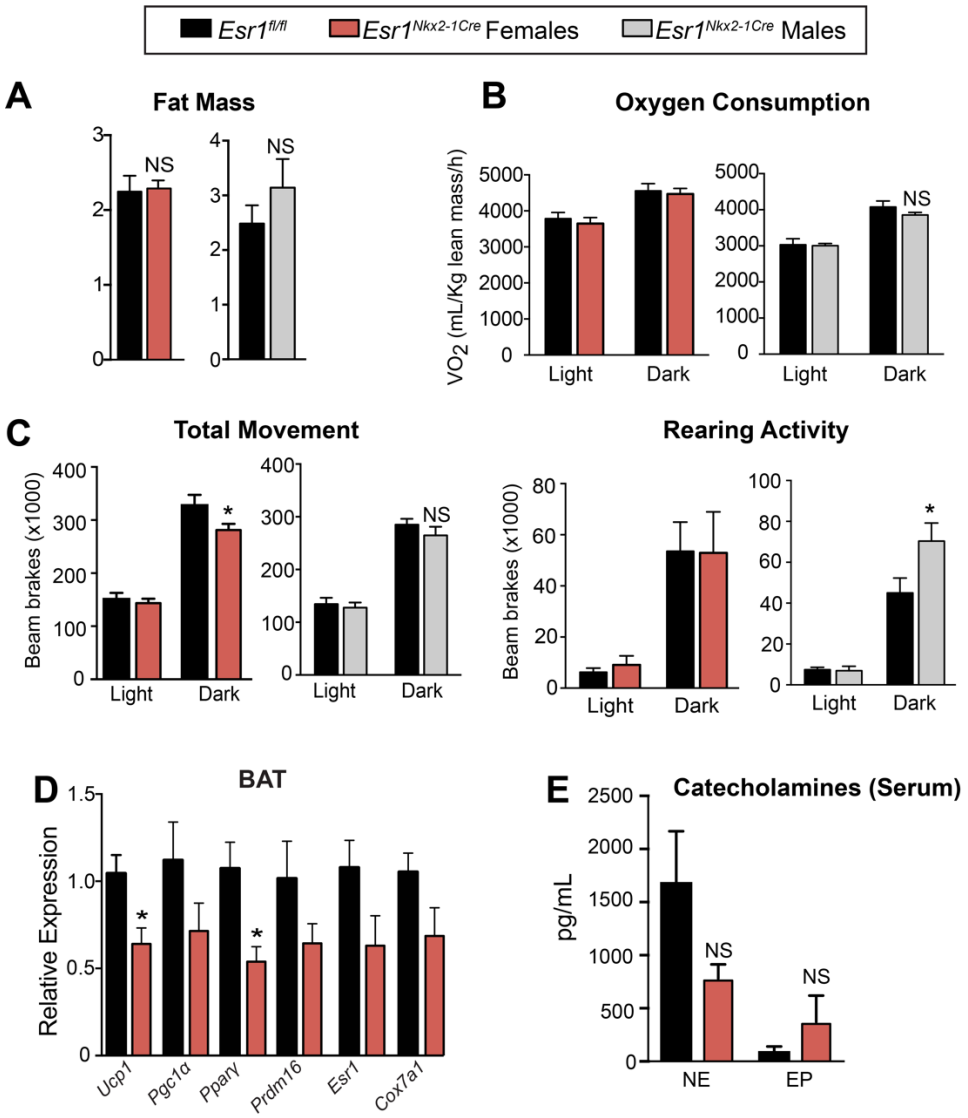

Fig. S2. Lower movement and markers of BAT in female *Esr1*$^{Nkx2\text{-}1Cre}$ mice.

(**A**) Fat mass determined by EchoMRI. Metabolic chamber analyses of energy expenditure including (**B**) oxygen consumption (VO2) normalized to grams of lean mass, (**C**) and activity as measured by average total movement (beam brakes, x and y axis) ($F_{1,14}$ = 4.2, *p < 0.05) and cumulative rearing activity (beam brakes, z axis) per animal for 12 h shown for *Esr1*$^{fl/fl}$ and *Esr1*$^{Nkx2\text{-}1Cre}$ females and males. (**D**) Levels of *Ucp1* transcripts and other BAT markers in control and mutant female mice at 22°C (n = 6 controls and n = 8 mutants). (**E**) Serum norepinephrine (NE) and epinephrine (EP) concentrations in controls (n = 4) and mutant female mice (n = 6). Unless otherwise stated, all experimental groups (n = 11, 9) females and

(n = 4, 5) males for controls and mutants, respectively. Error bars ± SEM. Students t-test for Panels A, D and E. Two-way ANOVA for Panels B and C.

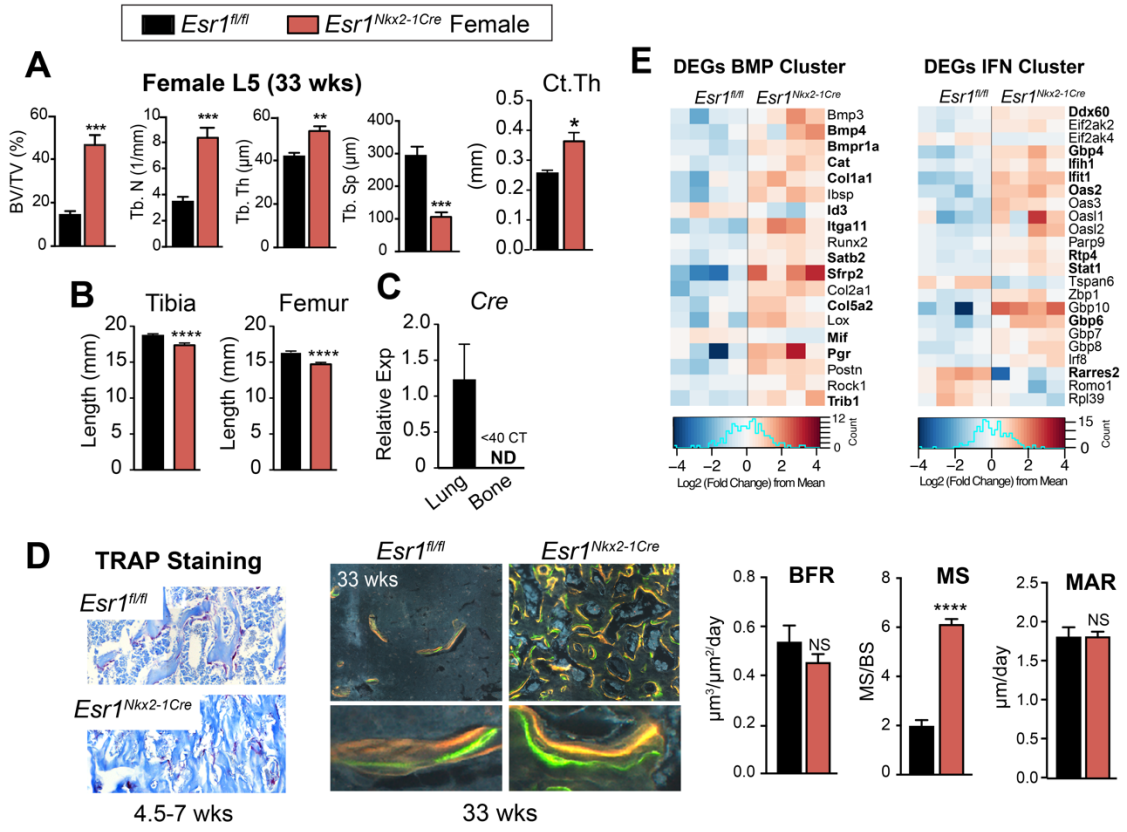

Fig. S3. *Esr1*$^{Nkx2\text{-}1Cre}$ mice exhibit increased bone and BMP/Interferon signaling.
(**A**) Morphometric properties of L5 vertebrae from 33-wk old *Esr1*$^{fl/fl}$ (n = 4) compared to *Esr1*$^{Nkx2\text{-}1Cre}$ (n = 4) female mice as analyzed by μCT. Cortical thickness at the TBJ measured by μCT in 20 wk old females in control and mutants (n = 3, 3). (**B**) Morphometric analyses of tibial and femoral length of *Esr1*$^{fl/fl}$ (n = 5) and *Esr1*$^{Nkx2\text{-}1Cre}$ (n = 8) female mice. (**C**) *Cre* expression in lung and femoral bone of female mice. (**D**) Representative images of TRAP staining in femurs from young females, and from calcein (green) and demeclocycline (orange) labeled femurs with quantified BFR, MS and MAR for older *Esr1*$^{fl/fl}$ (n = 8) and *Esr1*$^{Nkx2\text{-}1Cre}$ (n = 5) females. (**E**) Heat maps of two DEG clusters representing BMP and IFN signaling upregulated in mutant *Esr1*$^{Nkx2\text{-}1Cre}$ female bone marrow at 4.5 wks of age; scale bars are shown below heap maps. Error bars ± SEM. Statistical analyses performed using Student's *t*-test, *p < 0.05; **p < 0.01; ***p < 0.001.

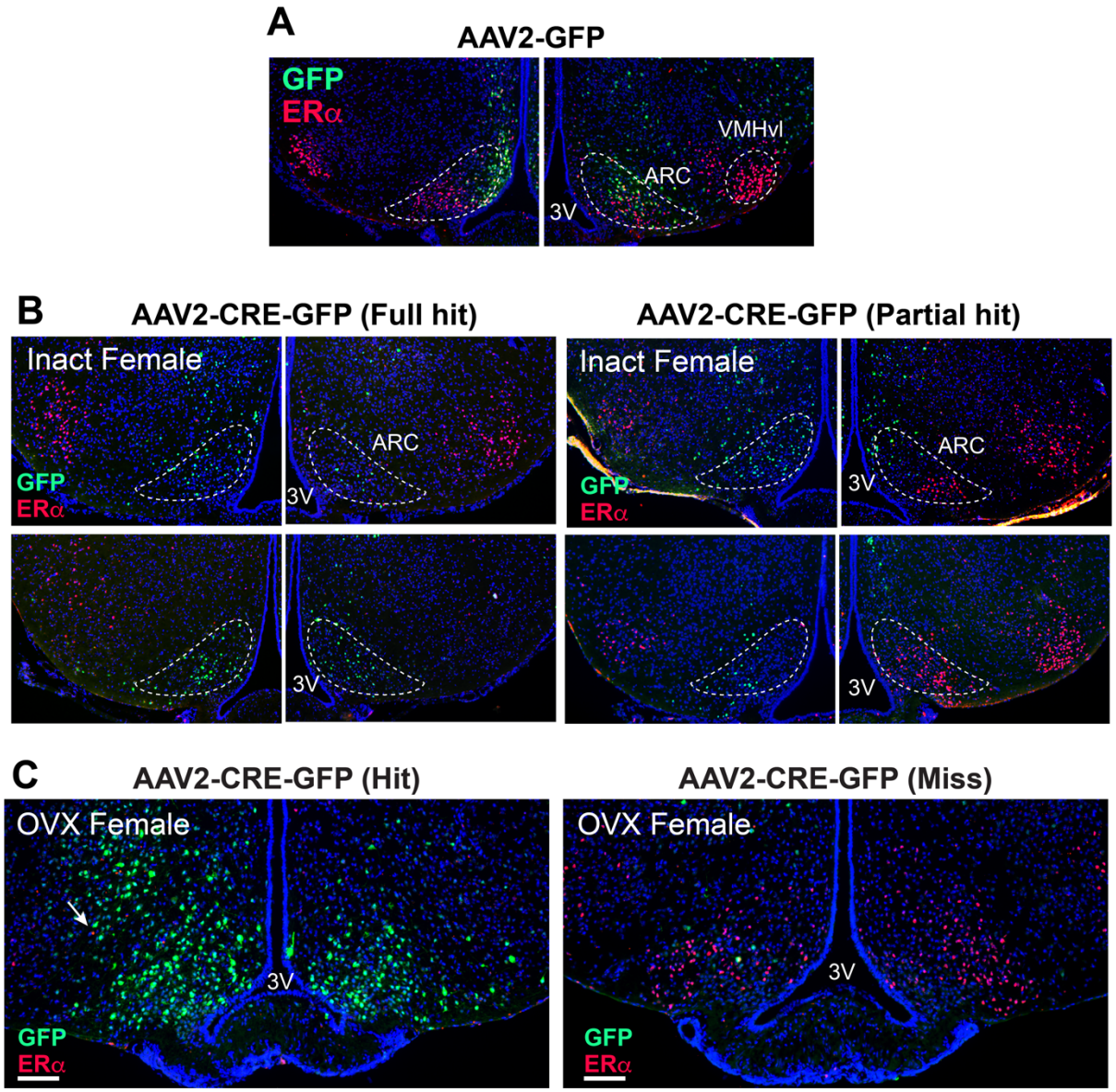

Fig. S4. Confirmation of ARC specific ablation of ERα in Intact and OVX ERαKO^{ARC} females.

Representative images of ERα (red) and GFP (green) immunoreactivity shown for coronal brain sections (20 μm) to assess the extent of ERα ablation in the ARC (**A**) control (AAV2-GFP) or (**B**) AAV2-Cre-GFP (ERαKO^{ARC}) of intact females or from (**C**) estrogen-depleted OVX females. Representative images are shown for a Control, Full or Partial Hits in intact females (28 wks) and for a Hit or Miss in OVX females (~38 wks). Scale bar = 100 μm.

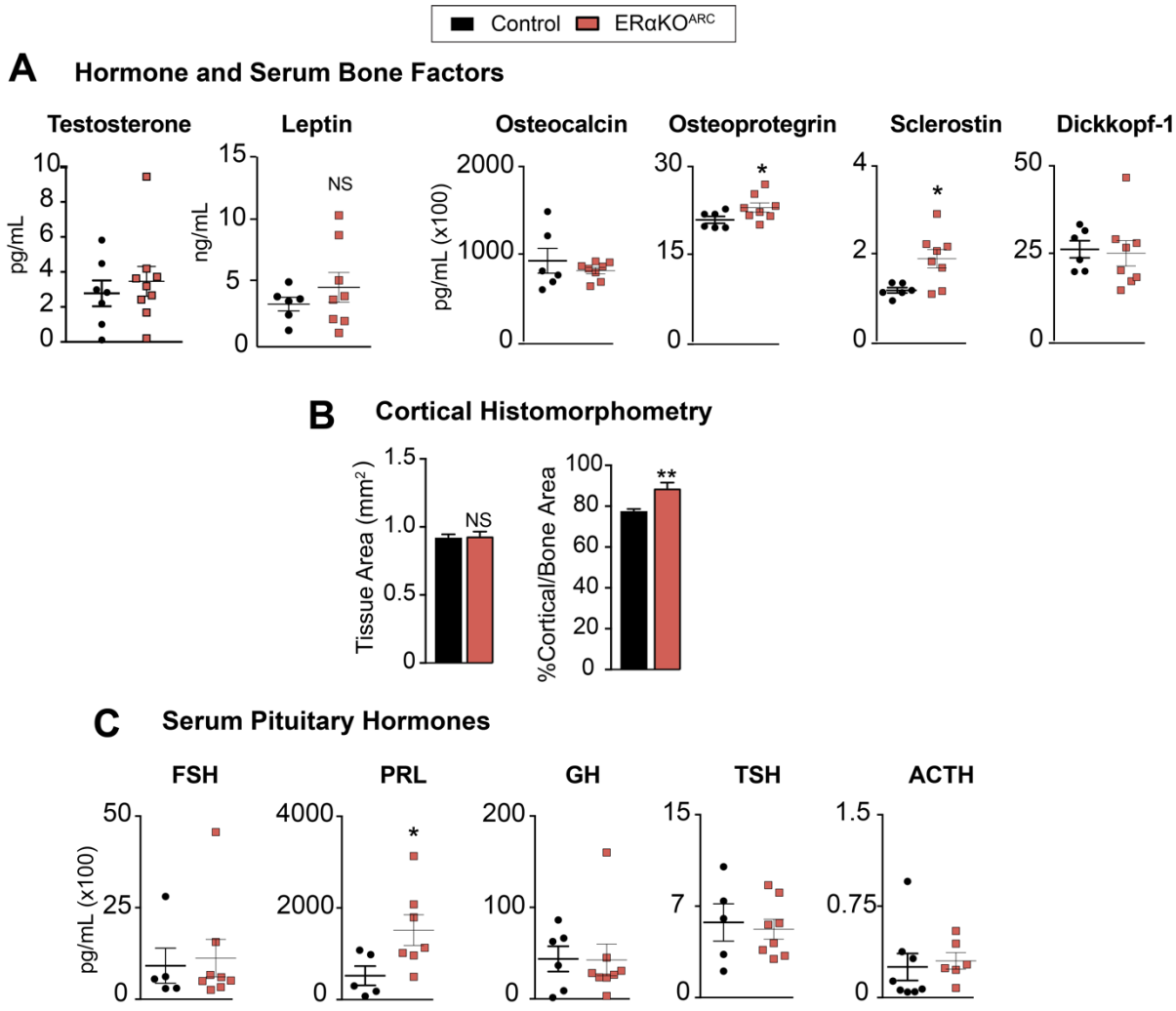

Fig. S5. Elevation in some cortical bone and serum factors in ERαKO^{ARC} females. (**A**) LC-MS/MS measurement of testosterone and ELISA quantification of circulating leptin and serum bone factors for control and ERαKO^{ARC} females 12 wks post viral infection. (**B**) Morphometric analysis of cortical bone at the tibio-fibular joint in controls (n = 4) and ERαKO^{ARC} (n = 4) females. (**C**) Levels of circulating pituitary hormones (pg/ml x 100) comparing control and ERαKO^{ARC} females 12 wks post viral infection. Error bars ± SEM. Statistical analyses performed by Student's *t*-test, *p < 0.05; **p < 0.01.

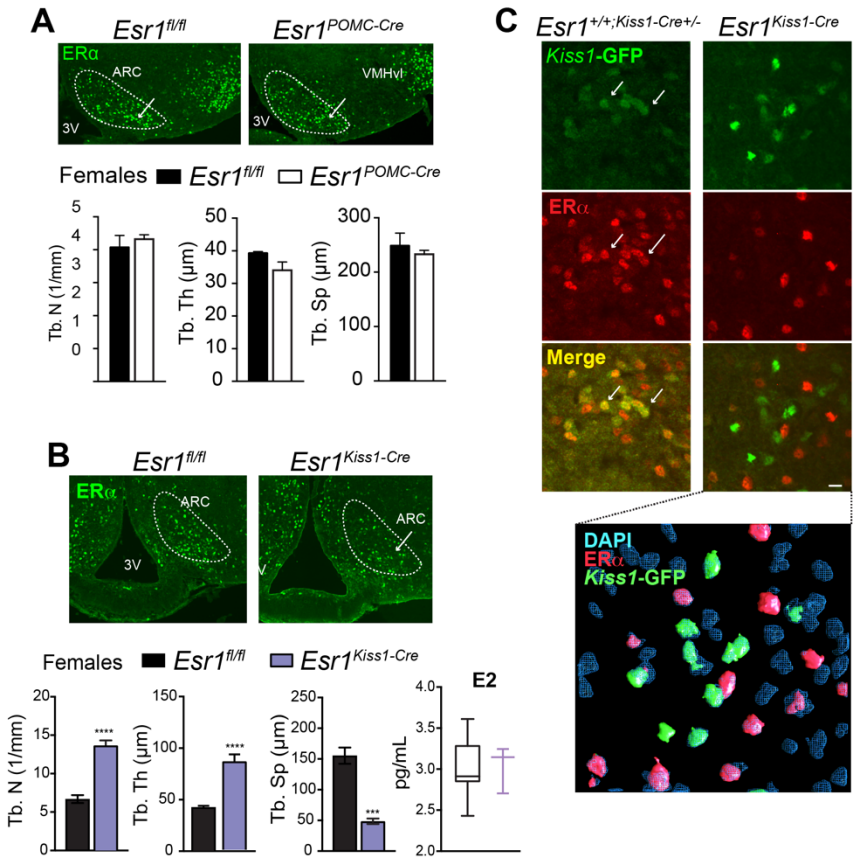

Fig. S6. Increased bone mass in *Esr1*$^{Kiss1\text{-}Cre}$ but not *Esr1*$^{Pomc\text{-}Cre}$ mice.
(**A)** Representative images of ERα (green) immunoreactivity shown for 20 μm coronal brain sections for *Esr1*$^{fl/fl}$ and *Esr1*$^{Pomc\text{-}Cre}$ and μCT quantitative morphometric indices for distal femur (n = 3 controls and 3 mutants). (**B**) Representative images of ERα (green) immunoreactivity shown for coronal brain sections for *Esr1*$^{fl/fl}$ and *Esr1*$^{Kiss1\text{-}Cre}$ with morphometric indices of distal femur (n =11 controls and 4 mutants). (**C**) Representative fields of ERα (red), GFP (green) and merged (Merge) images from ARC of *Esr1*$^{+/+}$*;Kiss1-Cre-GFP*$^{+/-}$ controls and *Esr1*$^{fl/fl}$*; Kiss1-Cre-GFP*$^{+/-}$ (*Esr1*$^{Kiss1\text{-}Cre}$) mutant females. Scale bar = 10 μm. Magnified surface map demonstrating no overlap of nuclear ERα and GFP staining in the ARC of *Esr1*$^{Kiss1\text{-}Cre}$ mutant females. Error bars ± SEM. Statistical analyses performed by Student's *t*-test, **p < 0.01, ***p < 0.001, ****p < 0.0001.

Table S1. Gene Expression In Femoral Bone And Bone Marrow.

GENE	Femur (Mean ± SEM)		Bone Marrow (Mean ± SEM)	
	***Esr1*$^{fl/fl}$**	***Esr1*$^{Nkx2\text{-}1Cre}$**	***Esr1*$^{fl/fl}$**	***Esr1*$^{Nkx2\text{-}1Cre}$**
Adbr2	1.1 ± 0.41	0.74 ± 0.17	2 ± 0.74	0.97 ± 0.1
Adiponectin	30 ± 17	49 ± 14	5 ± 4.1	0.16 ± 0.01
Aggrecan	3.1 ± 1.3	14 ± 4.9	2 ± 1	196 ± 79
Axin	1.6 ± 0.33	2.9 ± 0.47	2.2 ± 1.50	0.24 ± 0.07
Cebpa	3.8 ± 2.8	15 ± 4.9	0.78 ± 0.22	0.33 ± 0.04
Col2a1	0.77 ± 0.16	3.4 ± 1	0.85 ± 0.28	0.3 ± 0.08
Lepr	0.99 ± 0.08	1.6 ± 0.21	1.1 ± 0.16	0.32 ± 0.07*
Pdgf1b	1.5 ± 0.26	3.6 ± 1	0.98 ± 0.32	0.52 ± 0.39
Pparγ	0.74 ± 0.31	1.7 ± 1.1	0.33 ± 0.33	ND
Runx2	0.93 ± 0.07	1.5 ± 0.36	1.0 ± 0.18	2.6 ± 0.62*
Sp7	1.2 ± 0.30	5.7 ± 1.5*	1.1 ± 0.24	5.2 ± 3.8
Tcf7	0.77 ± 0.13	1.3 ± 0.48	0.62 ± 0.31	0.49 ± 0.15
Wnt6	54 ± 49	2.2 ± 1.7	2 ± 1	0.07 ± 0.03
Wnt10a	11 ± 7.5	10 ± 5.1	1.1 ± 0.2	0.51 ± 0.1
Rankl	1.0 ± 0.09	1.2 ± 0.14		
Esr1	1.0 ± 0.10	0.96 ± 0.14		

Table S2. PCR Primers for Genotyping

Allele	Forward	Reverse
Esr1$^{fl/fl}$	TGGGTTGCCCGATAACAATAA	AAGAGATGTAGGGCGGGAAAA
Gt(ROSA)26Sor(CAG-tdTomato)	AAGGGAGCTGCAGTGGAGTA	CCGAAAATCTGTGGGAAGTC
	WT allele AAGGGAGCTGCAGTGGAGTA	WT allele CCGAAAATCTGTGGGAAGTC
		Reporter Reverse GGCATTAAAGCAGCGTATCC
Nkx2-1Cre	CCACAGGCACCCCACAAAAAT	GCCTGGCGATCCCTGAACAT
Pomc-Cre	WT allele TGGCTCAATGTCCTTCCTGG	CACATAAGCTGCATCGTTAAG
	Cre Allele GAGATATCTTTAACCCTGATC	
Kiss1-Cre	GACCTAGGCTCTGGTGAAGTA	WT allele AGCCTCCAGTGCTCACAGCAG
		Cre allele CTTGCGAACCTCATCACTCGTTGC
Dat-Cre	TGGCTGTTGGTGTAAAGTGG	WT allele GGACAGGGACATGGTTGACT
		Cre Allele CCAAAAGACGGCAATATGGT
TH-Cre	GAG ACA GAA CTC GGG ACC AC	AGG CAA ATT TTG GTG TAC GG

Table S3. Primer Pairs and Probes

RT-qPCR Primers

Gene	Forward Primer	Reverse Primer
Ucp1	CACGGGGACCTACAATGCTT	TAGGGGTCGTCCCTTTCCAA
Pgc1α	CAGTACAGCCCCGATGACTC	GAAAGCTCGTCCACGTCAGAC
Pparγ	CGGGCTGAGAAGTCACGTT	TGTGTCAACCATGGTAATTTCAG
Prdm16	GAAGTCACAGGAGGACACGG	TCATTGCATATGCCTCCGGG
AdBr3	GGAAGCTTGCTTGATCCCCA	GCCGTTGCTTGTCTTTCTGG
Esr1	GAACGAGCCCAGCGCCTACG	TCTCGGCCATTCTGGCGTCG
RankL	TATAGAATCCTGAGACTCCATGAAAAC	CCCTGAAAGGCTTGTTTCATCC
Kiss1	TGCTGCTTCTCCTCTGT	ACCGCGATTCCTTTTCC
Pdyn	AGCTTGCCTCCTCGTGATG	GGCACTCCAGGGAGCAAAT
mCyclo	TGGAGAGCAGCACCAAGACAGACA	TGCCGGAGTCGACAATGAT
36b4	GGCACCGAGGCAACAGTT	TCATCCAGCAGGTGTTTGACA

TaqMan Probes

Gapdh	Mm99999915_g1	*Rank*	Mm00437135_m1
Ppary	Mm01184323_m1	*Calcr*	Mm00432271_m1
C/ebpα	Mm00514283_s1	*Dkk1*	Mm00438422_m1
C/ebpβ	Mm00843434_s1	*Sost*	Mm00470479_m1
Adipoq	Mm00456425_m1	*Bglap*	Mm03413826_mH
Lepr	Mm00440181_m1	*Col1a1*	Mm0081666_g1
Pdgfr8	Mm00440701_m1	*Ccnd1*	Mm00432358_m1
Wnt10a	Mm00437353_m1	*Tcf7*	Mm00493445_m1
Wnt10b	Mm00442104_m1	*Sp7*	Mm00504574_m1
Wnt6	Mm00437353_m1	*Runx2*	Mm00501584_m1
Axin2	Mm00443610_m1	*Ctsk*	Mm00484036_m1